

# Evaluating the PurpleAir monitor as an aerosol light scattering instrument

James R. Ouimette<sup>1</sup>, William C. Malm<sup>2</sup>, Bret A. Schichtel<sup>3</sup>, Patrick J. Sheridan<sup>4</sup>, Elisabeth Andrews<sup>4,5</sup>, John A. Ogren<sup>6</sup>, W. Patrick Arnott<sup>7</sup>

<sup>1</sup>Sonoma Ecology Center, Eldridge, CA 95431, USA

<sup>2</sup>Cooperative Institute for Research in the Atmosphere, Colorado State University, Fort Collins, CO 80523, USA

<sup>3</sup>National Park Service Air Resources Division, Lakewood, CO 80225, USA

<sup>4</sup>NOAA Global Monitoring Laboratory, Boulder, CO 80305, USA

<sup>5</sup>Cooperative Institute for Research in Environmental Sciences, University of Colorado, Boulder, Colorado 80309, USA

<sup>6</sup>NOAA Global Monitoring Laboratory, Boulder, CO 80305, USA (Retired)

<sup>7</sup>Department of Physics, University of Nevada, Reno, NV 89557, USA

Correspondence to James R. Ouimette (JamesOuimette@sonomaecologycenter.org)

## Abstract

The Plantower PMS5003 sensors (PA-PMS) used in the PurpleAir (PA) monitor PA-II-SD configuration are equivalent to cell-reciprocal nephelometers using a 657 nm perpendicularly polarized light source that integrates light scattering from 18 to 166 degrees. Yearlong field data at the National Oceanic and Atmospheric Administration's (NOAA) Mauna Loa Observatory (MLO) and Boulder Table Mountain (BOS) sites show that the 1 h average of the PA-PMS first size channel, labeled ">0.3  $\mu\text{m}$ " ("CH1") is highly correlated with submicrometer aerosol scattering coefficients at the 550 nm and 700 nm wavelengths measured by the TSI 3563 integrating nephelometer, from 0.4  $\text{Mm}^{-1}$  to 500  $\text{Mm}^{-1}$ . This corresponds to an hourly average submicrometer aerosol mass concentration of approximately 0.2 to 200  $\mu\text{g m}^{-3}$ . A physical-optical model of the PA-PMS is developed to estimate light intensity on the photodiode, accounting for angular truncation of the volume scattering function as a function of particle size. The model predicts that the PA-PMS response to particles >0.3  $\mu\text{m}$  decreases relative to an ideal nephelometer by about 75% for particle diameters  $\geq 1.0 \mu\text{m}$ . This is a result of using a laser that is polarized, the angular truncation of the scattered light, and particle losses (e.g., due to aspiration) before reaching the laser. It is shown that CH1 is linearly proportional to the model-predicted intensity of the light scattered by particles in the PA-PMS laser to its photodiode over 4 orders of magnitude. This is consistent with CH1 being a measure of the scattering coefficient and not the particle number concentration or particulate matter concentration. The model predictions are consistent with data from published laboratory studies which evaluated the PMS against a variety of aerosols. Predictions are then compared with yearlong fine aerosol size distribution and scattering coefficient field data at the BOS site. Field data at BOS confirm the model prediction that the ratio of CH1 to the scattering coefficient would be highest for aerosols with median scattering diameters <0.3  $\mu\text{m}$ . The PA-PMS detects aerosols smaller than 0.3  $\mu\text{m}$  diameter in proportion to their contribution to the scattering coefficient. The results of this study indicate that the PA-PMS is not an optical particle counter and that its six size fractions are not a meaningful representation of particle size distribution. The relationship between the PA-PMS 1 h average CH1 and  $b_{\text{sp}1}$ , the scattering coefficient in  $\text{Mm}^{-1}$  due to particles below 1  $\mu\text{m}$  aerodynamic diameter, at wavelength 550 nanometers, is found to be  $b_{\text{sp}1} = 0.015 \pm 2.07 \times 10^{-5} \times$

45 CH1, for relative humidity below 40%. The coefficient of determination  $r^2$  is 0.97. This suggests  
46 that the low-cost and widely used PA monitors can be used to measure and predict the submicron  
47 aerosol light scattering coefficient in the mid-visible nearly as well as integrating nephelometers.  
48 The effectiveness of the PA-PMS to serve as a  $PM_{2.5}$  mass concentration monitor is due both to  
49 the sensor behaving like an imperfect integrating nephelometer and to the mass scattering  
50 efficiency of ambient  $PM_{2.5}$  aerosols being roughly constant.

51 Keywords: PurpleAir, Plantower PMS5003, nephelometer, low-cost sensor, physical-optical  
52 model,  $PM_{2.5}$ , scattering coefficient, visibility, atmospheric aerosol

## 53 **1. Introduction**

54 Currently there are tens of thousands of low-cost aerosol monitors used by atmospheric research  
55 groups, air quality monitoring and regulatory organizations, and individual citizen scientists  
56 around the world. The recent explosion in the number of these sensors (see, for example, Aerosol  
57 Air Qual. Res. 20(2), 2020, Special Issue on Low-cost Sensors for Air Quality Monitoring and  
58 papers therein) is a result of the increased research, regulatory, and citizen interest over the past  
59 few years. For example, there are over 9,000 active PurpleAir (PA) aerosol monitors (PurpleAir  
60 LLC, Draper, UT), with sampling locations on almost every continent. The large geographic  
61 coverage of this array of low-cost sensors presents enormous potential for obtaining valuable  
62 information on atmospheric aerosol properties and transport processes.

63 The majority of these low-cost aerosol sensors are used to monitor the mass concentration of  
64 particles with aerodynamic diameters  $<2.5 \mu\text{m}$  ( $PM_{2.5}$ ) (Kelly et al., 2017; Gupta et al., 2018;  
65 Zheng et al., 2018; Sayahi et al., 2019; Barkjohn et al., 2020; Holder et al., 2020; Jayaratne et al.,  
66 2020; Malings et al., 2020; Mehadi et al., 2020). However, these sensors do not actually measure  
67 aerosol mass concentrations but light scattered by the aerosols and thus are dependent on the  
68 aerosol particle size distribution, morphology, and composition. Recently, Hagan and Kroll  
69 (2020) developed a framework and computer model to estimate the effects of relative humidity  
70 (RH) and aerosol refractive index on  $PM_{2.5}$  estimated by a number of low-cost sensors. Their  
71 model assumed that the low-cost sensor lasers were not polarized and could be modeled with  
72 Mie theory. The PMS5003 (PMS) was included in their classification scheme as an example of a  
73 sensor that behaved more like a nephelometer than an optical particle counter.

74 Three recent laboratory studies showed that the PMS response decreases with particle size. He et  
75 al. (2020) measured the PMS response to monodisperse ammonium sulfate aerosol particles  
76 having diameters of 0.1, 0.3, 0.5, and 0.7  $\mu\text{m}$ . The PMS was able to detect 0.1  $\mu\text{m}$  particles. They  
77 derived a transfer function that showed that the PMS  $>0.3 \mu\text{m}$  channel (CH1) response was  
78 maximum at particle diameter 0.26  $\mu\text{m}$  but decreased significantly below this size. They  
79 concluded that the PMS behaved more like a nephelometer than an optical particle counter.  
80 Kuula et al. (2020) generated monodisperse dioctyl sebacate oil droplets from 0.5 to 20  $\mu\text{m}$  and  
81 measured the PMS CH1 response versus particle diameter using an aerosol particle sizer (APS).  
82 Their data showed that the PMS relative response decreased for particles  $>0.5 \mu\text{m}$  diameter.  
83 Tryner et al. (2020) evaluated three low-cost particulate matter sensors, including the PMS, by  
84 exposing them to five different types of aerosols in the laboratory. They found that the ratios of  
85 PMS-reported to filter-derived  $PM_{2.5}$  mass concentrations were inversely proportional to mass  
86 median diameter (MMD). Wood smoke had the smallest MMD, 0.42  $\mu\text{m}$ ; its PMS  $PM_{2.5}$

87 averaged 2.5 times the filter-derived PM<sub>2.5</sub>. Conversely, oil mist had the largest MMD, 2.9 μm;  
88 its PMS PM<sub>2.5</sub> averaged only 0.23 times the filter-derived PM<sub>2.5</sub>.

89 Climate modeling requires a robust set of models and atmospheric measurements for predicting  
90 anthropogenic aerosol radiative forcing. Currently, there are uncertainties in the modeling  
91 results, due in part to the sparseness of ground-based data used to evaluate and refine the models  
92 (e.g., Gliss et al., 2021). Satellite observations provide global coverage that can be used for  
93 model evaluation, but satellite data require further assessment, particularly when trying to  
94 provide information about surface aerosol properties. The Surface Particulate Matter Network  
95 (SPARTAN) (<https://www.spartan-network.org/>; Snider et al., 2015) was specifically designed  
96 to assess and improve algorithms to relate satellite retrievals to surface aerosols. SPARTAN  
97 operates collocated filter-based PM<sub>2.5</sub>, aerosol scattering coefficient via nephelometer, and  
98 aerosol optical depth (AOD) measurements at approximately 20 sites around the world. Model  
99 and satellite uncertainties can be reduced using a distributed set of low-cost sensors that can  
100 provide aerosol light scattering estimates at a higher spatial and temporal resolution than is  
101 possible using nephelometers alone. Low-cost sensors are increasingly being used along with  
102 satellite data to estimate global aerosol impacts (Gupta et al., 2018).

103 There is ongoing scientific debate about the accuracy and precision of these low-cost sensors and  
104 their limitations (Morawska et al., 2018; Jayaratne et al., 2020). Many of the recent papers  
105 discuss performance evaluations or “calibrations” of these low-cost sensors by comparing their  
106 measurements with traditional, research-grade aerosol measurements (Papapostolou et al., 2017;  
107 Barkjohn et al., 2020). The concerns over data quality, stemming largely from inexpensive  
108 components, lack of transparency of signal processing, and inadequate quality control and testing  
109 at the factory, must be weighed against the advantages of low cost and wide spatial coverage.

110 The actual measurement in the PA monitor with its two PMS5003 sensors (PA-PMS), and in  
111 many other low-cost aerosol monitors, is of light scattered by particles integrated over a wide  
112 range of angles (Kelly et al., 2017), which has traditionally been done in atmospheric research  
113 and aerosol monitoring programs using integrating nephelometers. Aerosol light scattering and  
114 extinction measurements are useful in many applications, including determination of the  
115 radiative forcing effects of aerosols on climate change, atmospheric visibility, wildfire/smoke  
116 impacts, and validation of model outputs and satellite retrievals (e.g., Malm et al., 1994;  
117 Sherman et al., 2015; Snider et al., 2015; Gliss et al., 2021). Even though most low-cost aerosol  
118 sensors use light scattering as the basis of their operation, almost none have been evaluated as a  
119 low-cost nephelometer to estimate atmospheric light scattering. Markowicz and Chilinski (2020)  
120 conducted a 3 year evaluation of two low-cost sensors versus the Aurora 4000 polar integrating  
121 nephelometer at a site in southeastern Poland. They found that the mass concentration of  
122 particles with aerodynamic diameters <10 μm (PM<sub>10</sub>) from the DfRobot SEN0177 and the  
123 Alphasense OPC-N2 were highly correlated ( $r^2 > 0.89$ ) with the aerosol scattering coefficient  
124 measured by the nephelometer. They were able to estimate the 1 h average aerosol scattering  
125 coefficient from the low-cost sensors with a root mean square error (RMSE) of 20 Mm<sup>-1</sup>,  
126 corresponding to 27% of the mean aerosol scattering coefficient.

127 Unfortunately, due to cost, availability, and the expertise required to run them, integrating  
128 nephelometers are not operated in great numbers around the world. A recent analysis by Laj et  
129 al. (2020) showed 56 long-term monitoring stations reporting their nephelometer data to the

130 World Meteorological Organization (WMO) Global Atmosphere Watch (GAW) World Data  
131 Centre for Aerosols. This count includes nephelometers operated in several monitoring  
132 networks, including the National Oceanic and Atmospheric Administration’s (NOAA) Federated  
133 Aerosol Network (NFAN, Andrews et al., 2019), the Aerosols, Clouds and Trace Gases Research  
134 Infrastructure (ACTRIS) network (e.g., Pandolfi et al., 2018), and the Interagency Monitoring of  
135 Protected Visual Environments (IMPROVE) network (Malm et al., 1994). While there are more  
136 nephelometers in use around the world for short-term field and laboratory studies, the number  
137 almost certainly does not exceed a few hundred. This is small compared with the number of low-  
138 cost aerosol monitors in use globally.

139 This paper presents an evaluation of the performance characteristics of the low-cost PA-PMS  
140 monitor to measure the integrated aerosol light scattering coefficient. It is shown that the PA-  
141 PMS sensor configuration is similar to a cell-reciprocal nephelometer. A physical-optical model  
142 based on Mie theory and the PMS geometry is created that predicts scattered light intensity on  
143 the PMS photodiode and aerosol forward and backward light scattering truncation. PA-PMS  
144 measurements are compared to yearlong measured aerosol light scattering coefficients at  
145 NOAA’s Mauna Loa Observatory (MLO) in Hawaii and to measured and modeled aerosol light  
146 scattering coefficients and aerosol size distribution at the Boulder Table Mountain (BOS) site in  
147 Colorado. Finally, an empirical relationship is developed to estimate the submicron light  
148 scattering coefficient and its uncertainty from the PA-PMS data.

149 With a better understanding of what the PA measures, how it works, and its uncertainties, the  
150 large network of PA-PMSs could be used to estimate the submicrometer aerosol scattering  
151 coefficient at visible wavelengths throughout the world. These data could then be used to  
152 improve chemical transport and general circulation models, advance climate change predictions,  
153 and provide for better air quality forecasts.

## 154 **2. Instrument description**

155 In this section we first describe the physical and optical characteristics of the PA-PMS to place it  
156 in the context of nephelometry. We then provide a brief overview of integrating nephelometers,  
157 which are instruments designed specifically to measure light scattering.

### 158 **2.1 PA-PMS nomenclature**

159 The PMS sensor outputs 14 fields that are processed and reported by the PA. Each of these  
160 fields will be referred to as a channel. For instance, the PA-reported number concentration of  
161 particles  $>0.3 \mu\text{m}$  is referred to as CH1 in the remainder of this paper, number concentrations  
162  $>0.5 \mu\text{m}$  as channel two (CH2), and so forth. Furthermore, the two PMS sensors embedded in  
163 the PA will be referred to as either sensor A or sensor B. Therefore, the number concentration of  
164 particles  $>0.3 \mu\text{m}$  derived from sensor A will be referred to as CH1A and those from sensor B as  
165 CH1B. The average of CH1A and CH1B will be referred to as CH1avg. The PMS reports the  
166 CH1 units as “#/dl”, which is the number of particles having diameters  $>0.3 \mu\text{m}$  per deciliter. In  
167 this paper the PMS units for CH1 are not used.

### 168 **2.2 Description of the PA and its PMS 5003 sensors**

169 The PA monitor integrates two PMS sensors, a Bosch BME280 pressure, temperature, and RH  
170 sensor and an ESP 8266 chip (<https://www2.purpleair.com/pages/technology>). The PA-reported

171 temperature and RH are based on the sensor attached to the circuit board, and do not necessarily  
172 represent ambient conditions. The available specifications of the PMS are incomplete, and the  
173 processing algorithms are unknown (He et al., 2020). The following is based on available  
174 information and, where needed, professional judgment. Each PMS includes a small laser, a  
175 photodiode, a small fan to draw air across the laser beam, a microprocessor control unit (MCU),  
176 and probably an operational amplifier. The MCU processes the signal from the photodiode and  
177 outputs the following data fields approximately once per second:  $>0.3 \mu\text{m}$ ,  $>0.5 \mu\text{m}$ ,  $>1.0 \mu\text{m}$ ,  
178  $>2.5 \mu\text{m}$ ,  $>5 \mu\text{m}$ ,  $>10 \mu\text{m}$ ,  $\text{PM}_1$ ,  $\text{PM}_{2.5}$ , and  $\text{PM}_{10}$ . The PMS denotes the first six data fields as  
179 particle number concentrations above the designated cutpoint and the last three data fields as  
180 mass concentrations of particles below the designated cutpoints; the PM data fields are reported  
181 for two different conditions, “standard particles” and “under atmospheric environment”. The PA  
182 ESP8266 chip calculates 2 min averages of the PMS and BME280 signals. It transmits them  
183 wirelessly and writes them as a CSV file on a micro SD card.

### 184 **2.2.1 Airflow and particle losses**

185 The recommended orientation of the PA results in aerosol being drawn upward by a small fan  
186 through four 3 mm diameter entrance holes in each PMS. The aerosol then enters a  $9.4 \text{ cm}^3$   
187 chamber (Fig. S1a) and flows upward, parallel to and exposed to the circuit board as shown in  
188 Fig. S1b. Particles then make a 180 degree turn through three exit holes at the top of the chamber  
189 to emerge on the other side of the circuit board and flow downhill through a  $1.1 \text{ cm}^3$  channel that  
190 is illuminated by the laser. The total PMS volume is estimated to be  $9.4 + 1.1 = 10.5 \text{ cm}^3$ . The  
191 PMS volumetric flow rate is estimated to be  $1.5 \text{ cm}^3 \text{ s}^{-1}$  ( $\sim 0.090 \text{ lpm}$ ) based on measurements  
192 described in Supplemental Materials Sect. S1. The estimated inlet velocity through the entrance  
193 holes is estimated to be  $5.3 \text{ cm s}^{-1}$ .

194 The PMS inlet orientation 90 degrees to the wind, upward flow, and the low inlet velocity  
195 through the sampling holes can result in significant aspiration losses of larger particles (Hangal  
196 and Willeke, 1990). Aspiration losses are greater at higher wind speeds because it is more  
197 difficult for the larger particles to follow the streamlines into the low velocity PMS inlet. This  
198 can result in a lower concentration of larger particles entering the PMS than are in the ambient  
199 air. Particle aspiration losses are proportional to the particle Stokes number and the ratio of the  
200 wind velocity to the inlet face velocity (Hangal and Willeke, 1990). More details are provided in  
201 Supplemental Materials Sect. S1.

202 At typical wind velocities of  $1\text{--}3 \text{ m s}^{-1}$ , the ratio of PMS inlet face velocity to wind speed is only  
203 0.02 to 0.05, much lower than typical sampling ratios of 0.5 to 6.0 (Brockman, 2011). Pawar and  
204 Sinha (2020) addressed this problem for the Laser Egg low-cost sensor by putting it in a box and  
205 adding a 40 lpm fan to increase the inlet-to-wind velocity ratio and to direct the airflow upward  
206 to the Laser Egg inlet. During calm winds, large particle aspiration losses may occur by particle  
207 gravitational settling, acting against the PMS upward flow (Grinshpun et al., 1993). The actual  
208 wind conditions in the ambient air and in the PA near the PMS sample inlet are turbulent. Hangal  
209 and Willeke (1990) found in their wind tunnel experiments that turbulence intensity had a  
210 negligible effect on aspiration efficiency. Calculations using Eq. S1 (see Fig. S2) predict that at a  
211 wind speed of  $1 \text{ m s}^{-1}$ , the PMS aspiration losses for particles  $>2 \mu\text{m}$  may be significant.  
212 However, it must be cautioned that the literature does not include data for the very low  $5.3 \text{ cm s}^{-1}$

213 PMS face velocity, and actual measurements of the PMS aspiration efficiencies were not made.  
214 They may be significantly different from these calculated efficiencies.

215 Inside the PMS 9.4 cm<sup>3</sup> chamber, the air has an average velocity of 0.57 cm s<sup>-1</sup> and Reynolds  
216 number of 6.1, resulting in an average residence time of 6.3 s. The average air velocity in the  
217 chamber is equal to the sedimentation velocity of a spherical 10 μm diameter particle with a  
218 density of 2 g cm<sup>-3</sup> in air at STP (standard temperature and pressure; values used in this analysis  
219 are 273.15 K and 1013.25 hPa, respectively). This suggests that some 2 g cm<sup>-3</sup> density particles  
220 with diameters >10 μm that enter the PMS would settle out in the chamber and not make it to the  
221 three exit holes at the top of the chamber. Ultrafine particles can also be lost to the walls of the  
222 chamber and the printed circuit board due to convective diffusion. Calculations using the  
223 equation for diffusional losses (Friedlander, 1977) show that less than 1% of the 0.01 μm  
224 diameter aerosols would be lost in the chamber due to convective diffusion, with even smaller  
225 diffusional losses for larger particles.

226 Loss of particles due to inertial impaction on the wall opposite the three holes (Fig. S1b) was  
227 estimated by the local air flow Reynolds number near the three holes and the aerosol Stokes  
228 number. The local Reynolds number is calculated to be 23, and the Stokes number for 10 μm  
229 particles is  $8.2 \times 10^{-4}$ . At these low numbers, the calculated loss to impaction is less than 1% for  
230 all particles less than 10 μm diameter (Hering, 1995).

231 The average flow velocity through the laser beam is approximately 3.0 cm s<sup>-1</sup>. By the time the  
232 air flows through the laser beam, it has lost most of the particles over 10 μm diameter. Further  
233 particle losses due to gravitational settling over the photodiode would be very small, since the  
234 gravitational force is parallel to the photodiode.

235 In summary, it is likely that the laser in the PMS is sampling a lower concentration of particles >  
236 2 μm diameter than in the ambient air. Based on the literature and calculations, the dominant  
237 coarse aerosol loss mechanism may be aspiration, not internal losses. However, further  
238 measurements are needed to assess the various aerosol loss mechanisms.

### 239 **2.2.2 Laser**

240 The wavelength and power of three PMS diode lasers were measured using an Ocean Optics Red  
241 Tide USB650 spectrometer and Melles Griot Universal Optical Power Meter, respectively. The  
242 wavelength averaged 657 +/- 1 nm, and the power averaged 2.36 +/- 0.04 mW. The laser is  
243 polarized parallel to the plane of the photodiode detector. This results in the aerosol-scattered  
244 light being polarized perpendicular to the plane of incidence. Figure S3 shows that  
245 perpendicular polarization results in significantly greater scattering intensity from 0.3 μm  
246 particles compared to natural or parallel polarization. It is probable that many low-cost PM  
247 sensors have lasers that are polarized. Polarization will affect how the sensors respond to various  
248 size particles and needs to be considered when modeling sensor behavior.

249 The PMS laser beam profile is not a simple plane wave, but complex in shape. The laser has a 3  
250 mm diameter lens that focuses the laser over the photodiode. The beam profile evolves  
251 significantly as it goes through the focal region (Naqwi and Durst, 1990). The laser beam  
252 diameter in the laser sensing region over the photodiode was not measured. It was estimated by  
253 eye to be 0.5 to 1.0 mm, with significant uncertainty. The PMS MCU turns the laser on and off

254 every 800 msec or 2.5 s, depending on aerosol concentration. The laser pulses are 600–900  
255 msec, with the laser power on continuously during this time. We hypothesize that the PMS MCU  
256 gathers data during laser on, processes it during laser off, and uses the difference of the  
257 photodiode output during these stages to obtain and subtract any electronic or stray light (other  
258 than the laser) background signal to the photodiode.

### 259 **2.2.3 Photodiode detector**

260 The actual photodiode model in the PMS is unknown. The photodiode appearance is similar to  
261 the BPW34 silicon PIN photodiode. In this paper the specifications of the BPW34 are used to  
262 estimate the likely properties of the detector in the PMS. It has a very large dynamic range when  
263 operated with reverse bias. The dependence of the photodiode current on the light intensity is  
264 very linear over 6 or more orders of magnitude, e.g., in a range from a few nanowatts to tens of  
265 milliwatts. Silicon PIN photodiodes have low dark current, a 20 nanosecond rise time, and good  
266 wavelength sensitivity between roughly 400 and 1000 nm. ([https://www.rp-](https://www.rp-photonics.com/photodiodes.html)  
267 [photonics.com/photodiodes.html](https://www.rp-photonics.com/photodiodes.html)). At a wavelength of 657 nm, the BPW34 produces  
268 approximately 0.4 microampere current per microwatt of incident radiant power  
269 ([https://www.fiberoptics4sale.com/blogs/archive-posts/95046662-pin-photodetector-](https://www.fiberoptics4sale.com/blogs/archive-posts/95046662-pin-photodetector-characteristics-for-optical-fiber-communication)  
270 [characteristics-for-optical-fiber-communication](https://www.fiberoptics4sale.com/blogs/archive-posts/95046662-pin-photodetector-characteristics-for-optical-fiber-communication)). The PMS does not have any optical elements  
271 to capture and focus the aerosol-scattered light on its photodiode.

272 The photodiode does not have a cosine corrector in front and is probably not a true cosine  
273 detector. However, the relative spectral sensitivity is advertised to be a cosine response by the  
274 manufacturers  
275 ([https://www.osram.com/ecat/DIL%20BPW%2034%20B/com/en/class\\_pim\\_web\\_catalog\\_1034](https://www.osram.com/ecat/DIL%20BPW%2034%20B/com/en/class_pim_web_catalog_103489/prd_pim_device_2219537/)  
276 [89/prd\\_pim\\_device\\_2219537/](https://www.osram.com/ecat/DIL%20BPW%2034%20B/com/en/class_pim_web_catalog_103489/prd_pim_device_2219537/) and <https://www.vishay.com/docs/81521/bpw34.pdf>).

### 277 **2.2.4 Laser and photodiode geometry**

278 The PMS geometry is very similar to a cell-reciprocal nephelometer. Figure 1 shows the PMS  
279 laser and photodiode geometry. The measurements were made with a Brown & Sharpe  
280 micrometer. The distance from the laser exit hole to the photodiode is 2.5 mm; the perpendicular  
281 distance from the center of the laser beam to the photodiode is 1.8 mm; the diameter of the  
282 exposed photodiode area is 3.0 mm; the thickness of the base mask over the photodiode is 0.46  
283 mm; and the distance from the edge of the photodiode to the end of the laser sensing volume is  
284 4.5 mm.  $\theta_1$  is the lower angular scattering limit, and  $\theta_2$  is the upper angular scattering limit for a  
285 particle in the laser.

286 Due to the PMS geometry, the upper and lower angular scattering limits for  $\theta$  depend on the  
287 location,  $x$ , of a particle in the laser. This can be seen in Fig. S4. For example, at  $x = 0$  mm, at the  
288 laser exit, the upper and lower scattering limits for  $\theta$  are 18–38 degrees. At  $x = 4.0$  mm, over the  
289 center of the photodiode, the angular integration limits are 50–130 degrees. The PMS photodiode  
290 is not capable of detecting light scattered from particles at less than 18 degrees.

291 Figures S5–S9 provide more detail about the PMS dimensions and geometry.

### 292 **2.2.5 PMS5003 sensing volume**

293 The sensing volume is the volume in which the aerosol is irradiated by the laser. The sensing  
294 volume extends the length of the laser where the aerosol flows through it, approximately 10 mm.  
295 The sensing volume is shown in Fig. S9. The average residence time of a particle in the laser  
296 beam is approximately 30 ms. Some of the scattered light is detected by the photodiode and  
297 creates a voltage pulse approximately 30 ms wide. It appears that the photodiode is detecting  
298 either a cloud of particles from the sensing volume or individual pulses, depending on the  
299 concentration. At low concentrations, the aerosol concentration within the sensing volume is  
300 unlikely to be uniform, resulting in large relative changes in output per second.

### 301 **2.2.6 Signal processing and electronics**

302 It is not reported how the PMS MCU differentiates and processes the photodiode signals. The  
303 PMS MCU sends the PA a signal approximately every second in the form of a digital sequence  
304 of unsigned 16 bit binary data words, and CH1 is thought to be proportional to the photodiode  
305 current. The photodiode current was not measured in this study. The PA creates 80 s (Firmware  
306 Version 3) or 120 s (Firmware Version 4 and higher) averages and writes them to its micro SD  
307 card. We measured an average percentage difference of 0.3% between the 2 min averages  
308 reported by the PA and the 2 min averages calculated from the 1 s values from the PMS. The  
309 results are shown in Fig. S10. It is apparent that the processing done by the PA to calculate its  
310 reported 2 min averages does not bias the results.

### 311 **2.2.7 PMS CH1 variability in sampling filtered air**

312 We found significant variability in PMS response to filtered air. We exposed 21 PAs containing  
313 42 PMS sensors to filtered air for 2 to 94 hours. The results are summarized in Table S1. Hourly  
314 average CH1 ranged from 0.10 to 377. Eleven PAs had both PMS CH1A and CH1B averages  
315 below 2, while seven PAs had at least one CH1 average over 26. We recommend that before  
316 deployment the PAs sample filtered air for at least four hours to identify and eliminate PAs with  
317 CH1 hourly averages over 2 in filtered air. Removing PAs with high CH1 offsets in filtered air  
318 reduces uncertainty and improves precision, particularly in cleaner ambient air.

### 319 **2.2.8 PMS CH1 unresponsive to CO<sub>2</sub> and Suva<sup>®</sup>**

320 Filtered air, CO<sub>2</sub>, and Suva<sup>®</sup> (DuPont™ Suva<sup>®</sup> 134a refrigerant) are often used to calibrate  
321 integrating nephelometers (Anderson et al., 1996). The Rayleigh scattering coefficients of  
322 filtered air, CO<sub>2</sub>, and Suva at 657 nm and at STP (0 °C and 1013.25 hPa) are 5.5, 13.3, and 46.2  
323 Mm<sup>-1</sup>, respectively. We found that the PMS was unresponsive to 100% CO<sub>2</sub> (Fig. S11) and Suva.  
324 The CH1 for each gas was the same as filtered air. These results indicate that the PMS signal  
325 processing zeroes out a constant scattering signal and cannot be used to measure the scattering  
326 coefficient of gases that are commonly used in calibrating nephelometers. Furthermore, the  
327 method used by the PMS to subtract light scattering by air molecules in the sampling volume is  
328 unknown.

### 329 **2.2.9 PMS CH1 and CH1avg precision**

330 The PMS CH1 precision was measured by collocating ten PA monitors on the roof of the NOAA  
331 building in Boulder, Colorado, between 22 January 2021 and 1 February 2021. These monitors



332 were not checked with filtered air before deployment. It was found that two of the PMS sensors  
333 had large offsets and two had moderate offsets at low CH1 values. One PMS sensor was found to  
334 produce errant data and was removed from the analysis, resulting in valid data from 19 CH1A  
335 and CH1B sensors in the ten PAs.

336 The precisions for the hourly data from the CH1A and CH1B sensors and their average  
337 (CH1avg) were estimated as the coefficient of variation for each of the 19 CH1A and CH1B  
338 values and the 9 CH1avg values for each hour, which are plotted against the average CH1 values  
339 in Fig. 2. As shown, above CH1 values of 500, the precision is relatively constant with an  
340 average of 8% and 4.8% for CH1A-CH1B and CH1avg, respectively. Below CH1 values of 500,  
341 the uncertainties increase rapidly with decreasing CH1 values.

342 There are two mechanisms that may contribute to the rapid uncertainty increase for CH1 < 100.  
343 First, it is likely that some of the increased uncertainty in CH1 below values of 100 is inherent to  
344 sampling low concentrations, as is the case for any instrument. Second, the geometry of the laser  
345 sensing volume in the PMS can contribute to uncertainty in the CH1 at low concentrations,  
346 specifically if particles are not distributed uniformly within the laser beam.

347 The data in Fig. 2 can be modeled by the sum of squares of an additive ( $Un_{add}$ ) and multiplicative  
348 uncertainty ( $Un_{mult}$ ) (Currie, 1968; Hyslop and White, 2008; JCGM100:GUM, 2008):

$$349 \text{ Uncertainty} = \sqrt{Un_{add}^2 + Un_{mult}^2 * CH1} \quad (1)$$

350 Equation 1 was fitted to the precision data in Fig. 2 where the  $Un_{mult}$  was set to the average  
351 precision at high CH1 values, and  $Un_{add}$  was set to 28 and 19 for the A and B sensors and  
352 CH1avg, respectively, to fit the highest variances (Table S2). The  $Un_{add}$  is the precision of CH1  
353 as CH1 approaches zero and is assumed to be equivalent to the uncertainty in values below the  
354 instrument minimum detection limit (MDL) or that of blanks (Currie, 1968), which were 0.08  
355 and 0.048 for the A and B sensors and CH1avg, respectively. The coefficient of determination in  
356 the model fit for both sets of data was  $r^2 = 0.96$ . Defining the MDL as the 99% confidence  
357 interval of the  $Un_{add}$  (Code of Federal Regulations, 40 CFR 136, [https://ecfr.io/Title-40/Part-](https://ecfr.io/Title-40/Part-136)  
358 136), MDLs for the individual CH1 sensors and CH1avg were 65 and 44, respectively.

359 As shown in Sect. S3, the  $Un_{mult}$  and  $Un_{add}$  are highly dependent on the systematic biases  
360 between the individual CH1 sensors and CH1avg and the four CH1 sensors with data offsets as  
361 the CH1 approaches zero (Fig. S12). Removing these four sensors and normalizing the data for  
362 each CH1 sensor by its average reduced the  $Un_{add}$  and  $Un_{mult}$  to 9% and 3%, respectively, for the  
363 CH1 sensors and 6% and 1.9%, respectively, for the CH1avg data. These results correspond to  
364 an MDL of 21 and 14 for the normalized CH1 sensor and CH1avg data, respectively. Based on  
365 these results, an “off the shelf” PA will have a CH1avg MDL of about 44 and precision of less  
366 than 4.3%, but the careful selection of a PA without an offset and that has relatively low noise  
367 will have an MDL of 14 and precision of less than 1.9%.

### 368 **2.3 Overview of cell-direct and cell-reciprocal nephelometers**

369 The integrating nephelometer was invented during World War II (Beuttell and Brewer, 1949). It  
370 provides a direct measure of aerosol light scattering integrated over a large angular range, the  
371 “aerosol light scattering coefficient”. This measure requires no assumptions about aerosol

372 composition, size distribution, refractive index, or shape. The most common nephelometer  
373 configurations are the “cell-direct” and “cell-reciprocal”. Figure 3 presents schematics of the two  
374 types of nephelometers. The geometrical relationship between the laser and the photodetector in  
375 the PMS resembles a cell-reciprocal nephelometer (Fig. 3b).

376 Middleton (1952) was the first to show that the cell-direct nephelometer with a Lambertian  
377 (cosine-adjusted diffuser) light source directly measures the aerosol light scattering coefficient.  
378 Anderson et al. (1996), following the derivation in Butcher and Charlson (1972), added  
379 geometrical diagrams to make Middleton’s derivation much clearer. Mulholland and Bryner  
380 (1994) proved that the cell-reciprocal nephelometer with a Lambertian diffuser followed by a  
381 photodiode placed at the center of the cell-reciprocal nephelometer also directly measures the  
382 aerosol scattering coefficient. This put both the cell-direct and cell-reciprocal nephelometers on  
383 equal theoretical footing.

384 There are a number of cell-direct nephelometers in use today. They include the TSI 3563 (St.  
385 Paul, MN, USA; Anderson et al., 1996), the Ecotech Aurora Models 3000 and 4000 (Knoxfield,  
386 Australia; Müller et al., 2011), the Radiance Research M903 (Seattle, WA, USA; Heintzenberg  
387 et al., 2006), and the Optec NG-2 (Lowell, MI, USA; Molenaar, 1997). In contrast, cell-  
388 reciprocal nephelometers have more limited commercial availability. The photoacoustic  
389 extinctionmeter (PAX; Droplet Measurement Technologies, Inc., Longmont, CO, USA) and the  
390 three-wavelength photoacoustic soot spectrometer (PASS-3) use a cell-reciprocal nephelometer  
391 to measure the aerosol light scattering coefficient (Arnott et al., 2006). A cosine corrector  
392 followed by a photomultiplier tube is placed at the center of the cell-reciprocal nephelometer  
393 (Abu-Rahmah et al., 2006; Nakayama et al., 2015).

394 A “perfect nephelometer” is one in which the nephelometer is able to see the scattered light over  
395 the entire angular range from 0 to 180 degrees. In practice, this cannot be achieved for the cell-  
396 direct and cell-reciprocal nephelometers. Both the forward and backward scattering angles are  
397 truncated. For example, the TSI 3563 nephelometer has measured angular truncation below  
398 about 7 degrees in the forward direction and above 170 degrees in the backward direction  
399 (Anderson et al., 1996; Heintzenberg and Charlson, 1996). For the PASS-3, Nakayama et al.  
400 (2015) found that both the large effective truncation angle (21 degrees) as well as the  
401 perpendicular polarization of the 532 nm laser relative to the scattering plane contribute to the  
402 large particle size dependence of measured scattering. Light scattering from ammonium sulfate  
403 particles of 0.71  $\mu\text{m}$  diameter was reduced by 50% relative to a perfect nephelometer. Angular  
404 truncation generally results in nephelometers underestimating the contribution of particles larger  
405 than approximately 1  $\mu\text{m}$  diameter to the scattering coefficient, although corrections have been  
406 developed to account for angular nonidealities (e.g., Anderson and Ogren, 1998; Müller et al.,  
407 2011).

### 408 **3. A physical-optical model of the PMS5003**

409 To gain insight into how the PMS responds to ambient aerosol properties, a model was  
410 developed to estimate the intensity of scattered light impinging on the PMS photodiode. The  
411 primary purpose of the model was to predict how the PMS performance compares to other  
412 instruments designed to measure the aerosol scattering coefficient, such as integrating  
413 nephelometers. The model makes simplifying assumptions about the laser that allow the

414 application of Mie theory to the light scattered from particles in the laser. Details of the model  
 415 are presented in the Appendix.

416 The equation describing the intensity of light scattered from a particle in the laser is (Middleton,  
 417 1952; Anderson et al., 1996)

$$418 \quad I(\theta) = F_{dv} \beta_p(\theta) dv \quad (2)$$

419 where  $I(\theta)$  is the intensity of light at angle  $\theta$  scattered from a particle in the volume element  $dv$   
 420 (with units of  $W \text{ sr}^{-1}$ );  $\beta_p(\theta)$  is the volume scattering function ( $\text{m}^{-1} \text{ sr}^{-1}$ );  $F_{dv}$  is the incident laser  
 421 flux density ( $W \text{ m}^{-2}$ ) impinging on the volume element  $dv$ ; and  $dv$  is the volume element within  
 422 the laser.

423 The volume scattering function for a single particle in the laser beam is a function of aerosol  
 424 diameter  $D_p$ , complex refractive index  $m$ , laser wavelength  $\lambda$ , and scattering angle  $\theta$ :

$$425 \quad \beta_p(\theta) = (\lambda/2\pi)^2 (1/dv) |S_1(m, \lambda, \theta, D_p)|^2 \quad (3)$$

426 where  $|S_1(m, \lambda, \theta, D_p)|^2$  is the Mie scattering intensity function for laser light polarized parallel to  
 427 the photodiode surface and perpendicular to the plane of incidence (Bohren and Huffman, 1983).

428 The scattered light intensity from a single particle in the laser beam to a narrow strip across the  
 429 middle of the photodiode and from all positions in the scattering volume is integrated to predict  
 430 the total power received by the photodiode as a function of particle diameter  $D_p$  and refractive  
 431 index  $m$ :

$$432 \quad P(m, D_p) = K \int_{x=0}^{x=10mm} \int_{\theta_1(x)}^{\theta_2(x)} |S_1(m, \theta, D_p)|^2 \sin(\theta) d\theta dx. \quad (4)$$

433 Due to the PMS geometry, the upper and lower angular scattering limits for  $\theta$  depend on the  
 434 location,  $x$ , of a particle in the laser. Details are provided in the Appendix. This approach can be  
 435 used to estimate the amount of scattered energy detected from mixtures of particles of varying  
 436 diameters and indices of refraction, as shown in Eq. (5):

$$437 \quad P = K \int_{D_p} \int_{x=0}^{x=10mm} \int_{\theta_1(x)}^{\theta_2(x)} |S_1(m, \theta, D_p)|^2 \sin(\theta) N(D_p, m) d\theta dx dD_p. \quad (5)$$

### 438 **3.1 Model predictions - Deviation from a perfect cosine response**

439 As discussed above, the PMS has a photodetector that is about 1.8 mm below the laser, resulting  
 440 in forward scattering and backscattering truncation angles of 18 and 166 degrees, respectively.  
 441 Furthermore, the photodetector is recessed 0.46 mm below the scattering chamber base.

442 Equation 4 is used to explore the deviation from a perfect cosine response resulting from the  
 443 truncated scattering volume and recessed detector. It is shown in Fig. 4. For these calculations,  
 444  $S_1(m, \theta, D_p)$  is set equal to 1, which corresponds to isotropic scattering or a volume scattering  
 445 function that is constant over all scattering angles. It is assumed that the detector has a  
 446 Lambertian response, i.e., the light detected is independent of the direction of the incident  
 447 energy, which results in a detector cosine response. Figure 4 shows a perfect cosine response in

448 yellow, while the red line shows the deviation from a perfect cosine response due to angular  
449 truncation. The blue line shows the effect of both angular truncation and an inset detector that is  
450 0.46 mm below the chamber base. All curves have been normalized to one at 90 degrees.

### 451 **3.2 Model predictions - Intensity versus position on the detector**

452 Figure 5 provides an example of the energy distribution on the photodiode as a function of  
453 position in the laser and on the diode resulting from scattering from particles represented by a  
454 lognormally distributed aerosol volume size distribution with a volume mean diameter of 0.33  
455  $\mu\text{m}$  and geometric standard deviation of 1.7. Figure 5 shows model predictions of the relative  
456 intensity of scattered light, where the values are proportional to energy flux impinging on the  
457 detector.

458 The masking resulting from a recessed detector truncates the scattering both in the most forward  
459 and most backward scattering angles. This masking is shown as the triangular area  
460 corresponding to distance down the laser and detector of 0.0–2.5 mm and 0.0–0.78 mm,  
461 respectively, for the forward scattering angles and 5.6–10 mm and 1.44–3.0 mm, respectively,  
462 for backscattering. Because the laser is parallel to the photodetector, which is assumed to have a  
463  $\cos(90-\theta)$  response, the maximum energy scattered to the detector is approximately at  $\theta = 90$   
464 degrees. However, more energy is scattered to the detector for scattering angles less than 90  
465 degrees, which corresponds to forward scattering, and very little energy is detected by the  
466 photodiode for particles in the laser that are greater than about 8 mm down the laser beam, even  
467 though the detector is exposed to particles in the laser that are 10 mm away from the laser exit  
468 hole. These distances down the laser correspond to backscattering. The total energy detected by  
469 the photodiode is the sum or integral across both the detector surface and position in the laser  
470 and corresponds to the volume under the curve depicted in Fig. 5.

### 471 **3.3 Model predictions - Predicted photodiode response as a function of particle diameter**

472 The PMS differs from a perfect nephelometer in at least five important ways:

- 473 1. The laser is polarized, whereas the nephelometer light source is unpolarized.
- 474 2. The laser beam profile is not a simple plane wave, but complex in shape. The laser beam  
475 profile evolves significantly as it is focused over the photodiode.
- 476 3. The photodiode likely does not have a perfect cosine response.
- 477 4. The PMS geometry limits the photodiode to receiving scattered light between  
478 approximately 18 and 166 degrees, whereas a perfect nephelometer measures all energy  
479 scattered between 0 and 180 degrees.
- 480 5. The unknown PMS signal processing removes the light scattering signal from  $\text{CO}_2$ , Suva,  
481 and filtered air. These gases are used to calibrate nephelometers but cannot be used to  
482 calibrate the PMS.

483 The effects of these differences can be seen in Fig. 6, which shows predicted photodiode  
484 response as a function of particle diameter. The perfect nephelometer response is in blue, and  
485 the PMS response is in yellow. The red line predicts PMS response if the laser were not  
486 polarized. Relative intensities have been normalized to an ideal nephelometer measurement of a  
487 0.1  $\mu\text{m}$  diameter particle, which is akin to adjusting the laser power such that the scattered power  
488 at a diameter equal to 0.1  $\mu\text{m}$  is the same for all configurations. Scattering as a function of  
489 particle diameter is nearly the same for all three configurations from 0.1  $\mu\text{m}$  to about 0.3  $\mu\text{m}$ . At

490 about 0.8 to 1.0  $\mu\text{m}$ , the response of a PMS with an unpolarized laser is about half that of an  
491 ideal nephelometer, and the use of a polarized laser reduces its response to about 30% to that of  
492 an ideal nephelometer. For particles above 2  $\mu\text{m}$  in diameter, the PMS response compared to an  
493 ideal nephelometer is decreased by about 75%. Additionally, the PMS manual (Zhou, 2016)  
494 quotes a lower detection limit diameter of 0.3  $\mu\text{m}$ . The model predicts that particles smaller than  
495 0.3  $\mu\text{m}$  in diameter would be detected by the PMS, in direct proportion to their contribution to  
496 the scattering coefficient.

497 These differences in geometry and optics from an ideal nephelometer are further highlighted in  
498 Fig. 7. To highlight the effect of polarization, the blue line shows the ratio of an ideal  
499 nephelometer with a laser light source that is perpendicularly polarized to an ideal nephelometer  
500 with an unpolarized light source while the red line shows just the effect of PMS geometry  
501 relative to an ideal nephelometer. The yellow line shows the effects that polarization and PMS  
502 geometry have on the measured scattering signal. Again, all hypothetical instrument responses  
503 have been normalized to a particle diameter of 0.1  $\mu\text{m}$ . Relative to scattering for a 0.1  $\mu\text{m}$   
504 particle, the polarization alone reduces the scattering signal of an ideal nephelometer by 40% for  
505 particles with diameters in the 0.8–1.5  $\mu\text{m}$  size range. The additional effect of PMS scattering  
506 geometry reduces the scattering signal at 0.8–1.0  $\mu\text{m}$  by about another 30% relative to an ideal  
507 nephelometer.

508 As noted in Sect. 2.2.3, the specifications of the BPW34 are used to estimate the likely properties  
509 of the detector in the PMS. Our model assumes two ideal properties of the photodiode. The first  
510 is area uniformity - that a photon impinging any part of the photodiode would generate the same  
511 current as the same photon impinging on another part of the photodiode. The second ideal  
512 assumption is that the dependence of the photodiode current on the light intensity is very linear  
513 over 4 or more orders of magnitude. If these assumptions do not hold, then the yellow curve in  
514 Fig. 7 will change.

515 The variance in the PMS physical and optical geometry and errors in the measurements are not  
516 known but likely small. To evaluate the sensitivity of the modeled PA scattering to errors in  
517 these measurements, the model was exercised with large deviations of  $\pm 25\%$  and  $\pm 50\%$  in these  
518 inputs. As shown in Table S3, the errors tend to increase with particle size. The modeled PA  
519 scattering to a perfect nephelometer is most sensitive to errors in the distance from the laser to  
520 the photodiode. For particle diameters of 0.5  $\mu\text{m}$ , +25% and +50% changes in this distance  
521 resulted in maximum differences of 10% and 20%, respectively. Based on these results and the  
522 fact that the errors in the physical dimensions are less than 25%, these errors are thought to have  
523 a small contribution to the overall modeled PA scattering error and were not directly accounted  
524 for in the analysis. This analysis does not attempt to account for the possibility that the laser  
525 beam profile is not a simple plane wave or that the laser beam profile may evolve significantly as  
526 it is focused over the photodiode, and the standard plane wave Mie calculations would no longer  
527 apply.

### 528 **3.4 Model predictions – Differentiating by particle size**

529 The irradiance received by the PMS photodiode from a particle of a given diameter and  
530 refractive index depends on the particle's location in the laser beam. The model predicts that  
531 particles of different sizes may contribute the same irradiance to the photodiode, depending on

532 their location in the beam, or conversely, light scattered by a particle of a given size can vary by  
533 more than an order of magnitude.

534 As an example, the model predicts that all of the particles in Fig. 8 contribute the same irradiance  
535 to the PMS photodiode. The smaller particles contribute the same irradiance by scattering in the  
536 more effective forward scattering regime. The larger particles contribute the same irradiance by  
537 scattering in the less effective backscattering regime. The photodiode and its associated  
538 electronics would not be able to differentiate between them. As a result, the model predicts that  
539 the values reported in the six PA-PMS particle size channels from  $>0.3 \mu\text{m}$  to  $>10 \mu\text{m}$  cannot  
540 correctly represent the aerosol size distribution.

## 541 **4. Experimental – Field studies**

542 Field experiments were conducted at two of the NFAN aerosol monitoring stations: the Mauna  
543 Loa Baseline Observatory in Hawaii and the Table Mountain Test Facility in Colorado. Both  
544 sites have large suites of aerosol instrumentation and daily access for scientists and technicians to  
545 inspect, calibrate, and maintain the instruments. These sites also have integrating nephelometers  
546 (TSI 3563, St. Paul, MN, USA) against which to evaluate the PA monitors.

### 547 **4.1 Description of Mauna Loa site**

548 The Mauna Loa Baseline Observatory (MLO) is located on the north flank of the Mauna Loa  
549 volcano, on the Big Island of Hawaii ( $19.536^\circ\text{N}$ ,  $155.576^\circ\text{W}$ , 3397 m asl). The observatory is a  
550 premier atmospheric research facility that has been continuously monitoring and collecting data  
551 on global background conditions and atmospheric change since the 1950s  
552 (<https://www.esrl.noaa.gov/gmd/obop/mlo/>). Continuous aerosol measurements at MLO began in  
553 the mid-1970s with the installation of condensation particle counters and an integrating  
554 nephelometer (Bodhaine and Mendonca, 1974; Bodhaine et al., 1981). MLO lies above the  
555 strong marine temperature inversion layer present in the region, which separates the more-  
556 polluted lower portions of the island atmosphere in the marine boundary layer from the much  
557 cleaner free troposphere. MLO experiences a diurnal wind pattern (Ryan, 1997) that is strongly  
558 influenced by the daily heating and nighttime cooling of the dark volcanic lava rock that makes  
559 up the mountain. This “radiation wind” brings air up from lower elevations during the daytime,  
560 when atmospheric measurements reflect the local mountain environment. In contrast, during the  
561 nighttime, downslope winds develop, and the measurements at MLO are typically dominated by  
562 clean, free-tropospheric conditions (Chambers et al., 2013). At these times, the aerosol  
563 measurements at MLO often reflect some of the cleanest conditions at any station in the northern  
564 hemisphere. It has long been known, however, that episodic long-range transport of Asian  
565 pollution and dust aerosols occurs, most frequently in the springtime (Shaw, 1980; Miller, 1981;  
566 Harris and Kahl, 1990), and these aerosol events can influence both the daytime and nighttime  
567 measurements at MLO. Consequently, the aerosol levels at MLO vary over a large range, from  
568 extremely low to at times mildly elevated. Here we use observations from the MLO integrating  
569 nephelometer to evaluate the PMS sensor.

### 570 **4.2 Description of Boulder Table Mountain site**

571 The Table Mountain Test Facility (BOS) is a large restricted-access federal complex located 14  
572 km north of Boulder, Colorado ( $40.125^\circ\text{N}$ ,  $105.237^\circ\text{W}$ , 1689 m asl). NOAA conducts  
573 atmospheric research at this site, and in addition to its NFAN station, it is one of the Global

574 Monitoring Laboratory's seven U.S. Surface Radiation Network (SURFRAD) sites  
575 (<https://www.esrl.noaa.gov/gmd/grad/surfrad/tablemt.html>). Many instruments for measuring  
576 surface and column aerosol properties are maintained at this location and used for long-term  
577 monitoring of the atmosphere.

578 The BOS site lies just east of the Front Range foothills of the Rocky Mountains and is typical of  
579 a semi-arid, high plains environment. It is a high mesa of predominantly grassland with some  
580 desert scrub vegetation. The location is well suited for sampling of wildfire smoke plumes during  
581 fire season in the western United States (summer and autumn), dust events at any time of the  
582 year, and occasional urban pollution episodes. The NFAN station at BOS  
583 (<https://www.esrl.noaa.gov/gmd/aero/net/bos.html>) was completed in September 2019. BOS  
584 operates an integrating nephelometer and a differential mobility particle spectrometer (DMPS).  
585 Both provided useful data for evaluating some of the predictions from the physical-optical model  
586 we developed for the PMS sensor.

#### 587 **4.3 PA monitors**

588 PA-PMS monitors were installed on the aerosol towers at the MLO and BOS stations, just below  
589 the main aerosol inlets. MLO had two PA-PMS monitors, one gently heated and one unheated,  
590 whereas BOS had one gently heated PA-PMS monitor. Prior to deployment, the monitors were  
591 tested in a filtered air chamber for 4 hours to ensure that the 1 h average CH1 values were less  
592 than 1 when no particles were present. One of the PMS sensors in the unheated MLO PA had 1 h  
593 average CH1 values of 27 when no particles were present. The heated monitors were wrapped  
594 with heating tape and powered by small DC power supplies. All the monitors were covered with  
595 stainless steel flashing 5 cm below the bottom to prevent rain and snow from entering the inlet  
596 (Fig. S13).

597 The PA-PMS monitors were warmed in an effort to reduce the sample RH to be closer to that of  
598 the nephelometer, which is unavoidably heated to above ambient temperatures by the warmth of  
599 the laboratory and by the nephelometer's halogen lamp. Because of this warming, the RH inside  
600 the nephelometers rarely exceeded 40%. Both MLO and BOS are low-RH environments under  
601 normal conditions, although occasionally moist air masses are encountered. The heating of the  
602 monitors increased the sample temperatures by 5–8 °C, which helped to lower the sample RH.  
603 While the PA heating was not controlled to achieve an RH match with the nephelometer, it  
604 brought the sample RH of the two measurements closer together. The gentle warming of the  
605 heated PA to only a few degrees above ambient is unlikely to cause the PVC to off-gas or melt.  
606 Heating from direct sunlight may have had a larger impact.

607 Due to internet protocols at both sites, PA's wireless data transmission feature was not used, and  
608 the data were stored on the internal micro SD card. At approximately 1 month intervals, the data  
609 were downloaded from the micro SD cards, and the PAs were returned to service. Outputs from  
610 the two PMS sensors were then compared at these intervals to determine if the PAs were still  
611 functioning properly. In this study, the 80 s or 2 min averages were used to create 1 h averages to  
612 compare the PA observations to those of the nephelometer and the DMPS.

#### 613 4.4 Integrating nephelometer

614 The integrating nephelometer (TSI Inc., model 3563) measures the aerosol light scattering  
615 coefficient at three wavelengths (450, 550, and 700 nm). At both sites, the sample flow path is  
616 switched every 6 min between 1 and 10  $\mu\text{m}$  aerodynamic diameter, multijet, Berner-type  
617 impactors. Here, the scattering coefficients at 550 nm for both the  $\text{PM}_1$  and  $\text{PM}_{10}$  size fractions  
618 are used for comparison with the PMS measurements. These are referred to as  $b_{\text{sp}1}$  and  $b_{\text{sp}10}$ ,  
619 respectively.

620 There are two quality checks of the nephelometer operation made in the field. First, the  
621 nephelometer automatically samples filtered air once per hour. This provides a record of the  
622 stability of the instrument background measurement. Second, the nephelometer calibration is  
623 manually checked on a monthly basis using  $\text{CO}_2$  and filtered air (Anderson et al., 1996). The 1 h  
624 average  $b_{\text{sp}1}$  in filtered air is  $0.01 \text{ Mm}^{-1}$  with a standard deviation of  $0.12 \text{ Mm}^{-1}$ , based on 125  
625 hours of sampling filtered air.

626 The nephelometer measurements were corrected for angular truncation (Anderson and Ogren,  
627 1998) and reported at STP. Weekly data review provides quality assurance of the nephelometer  
628 data. Scattering coefficient data were averaged to 1 min resolution for logging and were further  
629 averaged to hourly resolution for comparison with the PA data. The 1 h average  $b_{\text{sp}1}$  uncertainties  
630 of the nephelometer measurements are  $\sim 0.13 \text{ Mm}^{-1}$  for scattering coefficients less than  $1.0 \text{ Mm}^{-1}$   
631 and  $\sim 10\%$  for scattering coefficients greater than  $1 \text{ Mm}^{-1}$  (Sherman et al., 2015).

#### 632 4.5 Differential mobility particle spectrometer (DMPS)

633 The DMPS was provided by the Institute for Atmospheric and Earth System Research,  
634 University of Helsinki, Finland. It was checked and calibrated by the World Calibration Centre  
635 for Aerosol Physics (WCCAP) at Leibniz Institute for Tropospheric Research (IfT), Leipzig,  
636 Germany, just prior to deployment at NOAA's Table Mountain site. After shipment from IfT to  
637 NOAA, the DMPS was again checked by aerosolizing polystyrene latex spheres and confirming  
638 that the peaks occurred in the correct size bins. The DMPS was housed inside the same building  
639 as the nephelometer at BOS and sampled aerosols through the same inlet, although the DMPS  
640 flow did not pass through the aerosol impactors.

641 The DMPS provides 40 channels of particle concentration versus size, ranging from mobility  
642 diameters of  $0.01 \mu\text{m}$  to  $0.8 \mu\text{m}$ . The  $0.1 \mu\text{m}$  to  $0.8 \mu\text{m}$  channels of the DMPS were used to  
643 calculate hourly average fine aerosol scattering coefficient distributions and the total fine aerosol  
644 scattering coefficient, assuming spherical particles (Mie theory) with a refractive index of  
645  $1.53+0.017i$ . The hourly average, DMPS-calculated fine aerosol scattering coefficients were  
646 compared to the nephelometer-measured fine aerosol scattering coefficients to check operational  
647 consistency (Fig. S14). No operational changes were made to the DMPS during this field study.  
648 This study did not measure coarse aerosol size distributions. The DMPS hourly average fine  
649 aerosol scattering coefficient distributions were used with the PMS physical-optical model to  
650 predict total 1 h average scattered irradiance on the photodiode.

### 651 5. Results

652 This section describes our evaluation of the PA-PMS using field data from MLO and BOS. First,  
653 we provide an overview of the observational data. We then assess how well the model described



654 in Sect. 3 is able to represent the observed data and show consistency with results previously  
655 reported in the literature. Next, we present results showing the potential of the PA-PMS to  
656 perform as a nephelometer. Finally, we note how the size information output by the PA is not  
657 correct due to the PA's primary measurement being a scattering measurement. For the results  
658 presented below, data from the PA-PMS, nephelometer, and DMPS were averaged to hourly  
659 frequency and merged prior to analysis.

## 660 **5.1 Field data overview**

661 Heated PA monitors were deployed at the MLO and BOS observatories for 15 and 11 months,  
662 respectively (Table 1). At both sites weather had no impact on the operation of the PA  
663 instrument, and downtime only occurred during data downloading.

664 These two deployments provide an excellent dataset for assessing PA performance in both a  
665 clean location (MLO) and in an environment with more elevated particle concentration (BOS).  
666 As shown in Table 2, during the field study at MLO, the median CH1 was 26.7. The median  $b_{sp1}$   
667 was  $0.76 \text{ Mm}^{-1}$  at 550 nm, which is approximately 10% of Rayleigh scattering at the MLO  
668 altitude. The reported  $\text{PM}_{2.5}$  mass concentration from the PA was zero for most of the MLO  
669 deployment. The CH1 and  $b_{sp1}$  are adjusted to STP in Table 2. The air quality at BOS was less  
670 pristine than at MLO and is more representative of nonurban continental air quality. The very  
671 high maximum CH1 and  $b_{sp1}$  at BOS reported in Table 2 occurred during smoke events in the  
672 summer and autumn of 2020. One of the BOS PMS sensors experienced approximately 10%  
673 degradation in sensitivity after one year in the field (Fig. S15).

## 674 **5.2 Relationship between model predictions and field data**

675 The PMS sensor is described by the manufacturer as a particle counter that measures particles  
676 between  $0.3 \mu\text{m}$  and  $10 \mu\text{m}$  in six size bins. Based on the theoretical characterization of the PMS  
677 sensor described in Sect. 3, the sensor is more akin to a polarized, reciprocal integrating  
678 nephelometer than a particle counter. Below, the field data and theoretical model are used to  
679 demonstrate that the raw PMS CH1 sensor signal is an integrated scattering measurement that is  
680 sensitive to particles smaller than  $0.3 \mu\text{m}$  but relatively insensitive to particles larger than  $1.0$   
681  $\mu\text{m}$ .

### 682 **5.2.1 Predicted photodiode irradiance versus CH1 field data at BOS**

683 Our model described in Sect. 3 and the Appendix predicts a value proportional to the scattered  
684 irradiance impinging on the PMS photodiode as a function of particle diameter and  
685 concentration. This was done using the DMPS size distribution data from BOS. The modeled  
686 PMS photodiode output is plotted against the PMS CH1 output (Fig. 9). The predicted  
687 photodiode output is linearly correlated with the ordinary least squares (OLS) regression ( $r^2 =$   
688  $0.90$ , normalized root mean square error (NRMSE)  $\sim 25\%$ ) with CH1 over 4 orders of magnitude.  
689 The RMSE contains contributions of errors from the model-predicted radiant power, the  
690 measured SMPS data the model is based on, as well as in the CH1 measurements. This strong  
691 correlation and low RMSE is convincing evidence that the model and SMPS data describe the  
692 PMS response quite well.

693 The linear relationship between CH1 and modeled photodiode response suggests the likelihood  
694 that the CH1 output is directly related to what the photodiode is sensing (i.e., scattering from all

695 particles in the scattering volume). The PA-PMS reported values, such as concentrations of  
696 particle numbers in various size ranges or PM concentrations, are quantities derived from the  
697 scattering signal and the use of an undescribed algorithm.

### 698 **5.2.2 Predicted aerosol size truncation versus published laboratory data**

699 The PMS physical-optical model described in Sect. 3 predicts that if CH1 is proportional to the  
700 photodiode power, then its signal will be reduced relative to a perfect nephelometer. Thus, the  
701 ratio  $CH1/b_{sp}$  should decrease as median scattering diameter increases. To test this prediction,  
702 data were obtained from published laboratory studies evaluating the PMS against aerosols of  
703 varying composition and size distribution reported by Tryner et al. (2020) and He et al. (2020).  
704 These reported aerosol size distributions were used here to calculate the aerosol scattering  
705 coefficient distributions from 0.1 to 10  $\mu\text{m}$  for the various aerosols and refractive indices at a  
706 wavelength of 657 nm. The median scattering diameter (MSD) was calculated for each test. The  
707 MSD is the aerosol diameter at which approximately half of the light scattering coefficient is due  
708 to particles smaller than the MSD and the other half to particles larger than the MSD. The MSD  
709 was then compared to the ratio of the measured CH1 and  $b_{sp10}$  values, i.e.,  $CH1_{avg}/b_{sp10}$ , for each  
710 of the tests reported in Tryner et al. (2020) and He et al. (2020). Figure 10 summarizes the  
711 results for  $CH1/b_{sp10}$  versus MSD.

712 The controlled laboratory results are in general agreement with the PMS physical-optical model,  
713 showing substantial reduction in  $CH1_{avg}/b_{sp10}$  as a function of increasing particle diameter from  
714 0.2 to 1  $\mu\text{m}$ . The laboratory results show an even greater reduction in  $CH1_{avg}/b_{sp10}$  than the  
715 model predicts at diameters larger than 1  $\mu\text{m}$ . This suggests the possibility of supermicron  
716 aerosol loss before laser detection, perhaps due to aspiration as discussed in Sect. 2.2.1.

### 717 **5.2.3 $CH1_{avg}/b_{sp1}$ as a function of median scattering diameter**

718 Although ambient aerosols may vary considerably in composition and morphology and cannot be  
719 as simply characterized as laboratory aerosols, it is instructive to evaluate if PMS angular  
720 truncation can be observed using field data. The DMPS data from BOS were used to calculate  
721 hourly average aerosol scattering coefficient distributions for diameters between 0.1  $\mu\text{m}$  and 0.8  
722  $\mu\text{m}$ . A wavelength of 657 nm and a particle refractive index of  $1.53+0.0i$  were used for the  
723 calculations. The median scattering diameter was calculated for each hour. The MSD was then  
724 compared to the ratio of the measured CH1 and  $b_{sp1}$  values, i.e.,  $CH1_{avg}/b_{sp1}$ , for each of these  
725 hours. The results are shown in Fig. 11 as a box and whisker plot of the  $CH1_{avg}/b_{sp1}$  values  
726 found in each MSD bin. The center MSD value for each bin is based on a logarithmic scale of  
727 MSD values where the upper and lower bin values are selected as  $MSD_i+MSD_{i+1}/2$  and  $MSD_i-$   
728  $MSD_{i-1}/2$  and  $i$  refers to the  $i^{\text{th}}$  bin. The thin black horizontal lines correspond to the number of  
729 observations in each bin and the scale is shown on the right hand axis. There are less than 20  
730 values in the 0.22  $\mu\text{m}$ , 0.63  $\mu\text{m}$ , 0.71  $\mu\text{m}$ , and 0.79  $\mu\text{m}$  bins. Approximately 67% of the MSDs  
731 observed at BOS were between 0.29  $\mu\text{m}$  and 0.36  $\mu\text{m}$ , and 98% of MSDs were between 0.26  $\mu\text{m}$   
732 and 0.46  $\mu\text{m}$ . The overall average  $CH1_{avg}/b_{sp1}$  ratio, based on 6777 observations, is 65 Mm.

733 Figure 11 is consistent with the PMS physical-optical model. The highest  $CH1_{avg}/b_{sp1}$  ratios  
734 tend to occur for aerosols with the lowest MSD and decrease as MSD increases. Additionally,  
735 the results show, as suggested above, that the PMS can detect particles below 0.3  $\mu\text{m}$  in diameter  
736 in proportion to their contribution to the scattering coefficient.

#### 737 5.2.4. Estimating the scattering coefficient minimum detection limit of the PA-PMS

738 The precision analysis in Sect. 2 indicates that the PA monitors used in this study estimated 1 h  
739 average CH1 and CH1avg MDLs of approximately 21 and 14, respectively. The estimated 1 h  
740 average MDL  $b_{sp1}$  of the TSI 3563 nephelometer is approximately  $0.20 \text{ Mm}^{-1}$ , based on filtered  
741 air tests. Further analysis of the relationship between CH1 and  $b_{sp1}$  at low levels was performed  
742 by plotting the ratio,  $\text{CH1avg}/b_{sp1}$ , for the combined MLO and BOS dataset, as a function of  $b_{sp1}$ .  
743 This relationship is shown graphically in Fig. 12. The data values were first averaged over 6  
744 hours because hourly  $b_{sp1}$  values near zero included many small negative  $b_{sp1}$  values due to the  
745 very clean conditions occasionally observed at MLO. The averaging eliminated all but five  
746 negative  $b_{sp1}$  values, which were removed from the dataset. The  $\text{CH1avg}/b_{sp1}$  and  $b_{sp1}$  values  
747 were further averaged over six data points after sorting the data on  $b_{sp1}$  levels to more clearly  
748 show the relationship between CH1avg and  $b_{sp1}$ . At  $b_{sp1} > 5 \text{ Mm}^{-1}$ , the  $\text{CH1avg}/b_{sp1}$  ratio is  
749 relatively constant at 67 Mm, the yellow line in Fig. 12. The yellow line is the slope of CH1avg  
750 versus  $b_{sp1}$  at  $b_{sp1}$  values greater than  $5 \text{ Mm}^{-1}$ . The  $\text{CH1avg}/b_{sp1}$  ratio systematically decreases  
751 from its highest values to about 35 Mm, the slope of CH1avg versus  $b_{sp1}$  at  $b_{sp1} = 0.4 \text{ Mm}^{-1}$ . For  
752  $b_{sp1} < 0.4 \text{ Mm}^{-1}$  the  $\text{CH1avg}/b_{sp1}$  ratio then increases significantly as  $b_{sp1}$  decreases, consistent  
753 with CH1avg values staying approximately constant below  $0.4 \text{ Mm}^{-1}$ . Both the CH1avg and  $b_{sp1}$   
754 are below MDL for  $b_{sp1} < 0.2 \text{ Mm}^{-1}$ . A  $\text{CH1avg}/b_{sp1}$  ratio of approximately 35 Mm at  $b_{sp1} = 0.4$   
755  $\text{Mm}^{-1}$  and a CH1avg value of about  $14 \pm 5$  is consistent with the estimated CH1avg MDL of 14.

756 Based on these results, the 1 h average CH1 sensor MDL for hourly data in units of scattering is  
757 approximately  $0.4 \text{ Mm}^{-1}$  at MLO. Laboratory tests challenging the PAs with known low-level,  
758 spiked aerosol concentrations and defined size distributions are needed to further refine the  
759 estimated MDL.

#### 760 5.2.5 Evaluating the use of the PA-PMS as an integrating nephelometer

761 The MLO and BOS hourly average CH1avg are plotted against  $b_{sp1}$ , measured at 550 nm, in Fig.  
762 13. Also shown in Fig. 13 is an OLS regression line with the intercept set equal to zero using the  
763 BOS and MLO combined dataset but with values associated with  $b_{sp1}$  less than  $0.4 \text{ Mm}^{-1}$  and  
764 greater than  $500 \text{ Mm}^{-1}$  removed. Results of the regression for the combined datasets as well as  
765 for the individual BOS and MLO datasets are presented in Table 3. There is good agreement for  
766 both datasets (Table 3) with an  $r^2$  of 0.97 and 0.85 for the BOS and MLO datasets, respectively,  
767 and 0.97 for the combined datasets. The relationship deviates somewhat from linear with  
768 increasing slopes and scatter at lower values of atmospheric scattering coefficient, particularly  
769 for the MLO data. The slopes (in  $\text{Mm}^{-1}$ ) for all data, MLO, and BOS, are  $0.015 \pm 2.07 \times 10^{-5}$ ,  
770  $0.017 \pm 5.72 \times 10^{-5}$ , and  $0.015 \pm 2.68 \times 10^{-5}$ , respectively. In the following analysis, a PA-derived  
771 atmospheric scattering ( $b_{sp1,PA}$ ,  $\text{Mm}^{-1}$ ) for both MLO and BOS is estimated using  $b_{sp1,CH1} = 0.015$   
772  $\times \text{CH1avg}$  at a wavelength of 550 nm. The best-fit value of  $0.015 \text{ Mm}^{-1}$  corresponds to the  
773 yellow horizontal line in Fig. 12 of 67.0 ( $1/0.015$ ) and corresponds to a median scattering  
774 diameter of about  $0.33 \mu\text{m}$  (Fig. 11).

775 Figure S16 shows that the submicron aerosol scattering coefficients at 550 nm and 700 nm are  
776 highly correlated, with the 700 nm scattering coefficient averaging 52% of the 550 nm scattering  
777 coefficient. This results in  $b_{sp1,CH1} = 0.0078 \times \text{CH1avg}$  at a wavelength of 700 nm.

778 As discussed above, the regression coefficient between  $b_{\text{sp1}}$  and CH1 for the combined dataset of  
779  $0.015 \text{ Mm}^{-1}$  is used to estimate the  $b_{\text{sp1,PA}}$  derived from the CH1 channel. The data for each  
780 dataset and the combined dataset were binned into ten bins based on measured  $b_{\text{sp1}}$  levels that  
781 ranged from  $0.4 \text{ Mm}^{-1}$  to  $500 \text{ Mm}^{-1}$ . Values of  $b_{\text{sp1}}$  above  $500 \text{ Mm}^{-1}$  were removed from the  
782 dataset. For each bin the NRMSE between  $b_{\text{sp1,PA}}$  and measured  $b_{\text{sp1}}$  was calculated. The  
783 NRMSE values as a function of the  $b_{\text{sp1}}$  bins are plotted in Fig. 14 for the combined dataset  
784 represented as the gray bars and BOS and MLO represented by blue and orange bars,  
785 respectively.

786 For  $b_{\text{sp1}}$  levels less than  $0.8 \text{ Mm}^{-1}$ , the NRMSE is 45–55%, and for  $b_{\text{sp1}}$  levels greater than  $10$   
787  $\text{Mm}^{-1}$ , the NRMSE is about 25% or less. For  $b_{\text{sp1}}$  levels greater than  $60 \text{ Mm}^{-1}$ , the NRMSE  
788 approaches 15%.

789 As discussed in Sect. 2.2.9, the uncertainty for high CH1 avg values is small (1.9% to 4.8%). The  
790 precision of the TSI 3563 nephelometer is also similarly high, and together they account for  
791 about 10% NRMSE at high  $b_{\text{sp1}}$  values.

792 The overall normalized error is likely due to a variety of sources, primarily the variability in the  
793 CH1 values due to using a polarized light source and truncation errors due to the geometry of the  
794 PA-PMS sensors. Also, the variability in aerosol characteristics such as size distribution,  
795 refractive index, and shape may be important. At extremely low levels, uncertainty may also be  
796 due to a nonuniform distribution of particles in the PMS laser beam.

797 There are two reasons why the PA-PMS MDL and RMSE values reported in our study are  
798 surprisingly low. The TSI 3563 nephelometer has an extremely low detection limit of  $0.20 \text{ Mm}^{-1}$ ,  
799 which is approximately 1% of Rayleigh scattering. Second, the PA-PMS has very low noise at  
800 zero aerosol concentration. If the PA in our study had been collocated with a nephelometer that  
801 was not as sensitive as the TSI 3563 in a location having an average fine aerosol coefficient of,  
802 say,  $30 \text{ Mm}^{-1}$ , then the PA 1 h average MDL could have been significantly higher than the  $0.4$   
803  $\text{Mm}^{-1}$  we obtained in our study.

#### 804 **5.2.6 PA-PMS size distributions**

805 The aerosol number concentrations from the six PMS size channels are unrealistic. The BOS  
806 field data showed that the concentration of particles larger than  $0.3 \mu\text{m}$  diameter calculated from  
807 the DMPS averaged 10 times higher than CH1 (Fig. S17). The other PMS size channels are so  
808 highly correlated with CH1 that they provide no additional information (Table S4). Furthermore,  
809 it appears that the PMS creates an approximately invariant normalized aerosol number  
810 distribution across a wide range of sites (Table S5, Fig. S18). Although the overall CH1  
811 concentration can vary over 6 orders of magnitude (column 3 in Table S5), the shape of the PMS  
812 size distribution remains fairly constant.

813 In our study, we found that the ambient aerosol size distributions measured with the SMPS  
814 varied considerably at Table Mountain, as seen in Fig. 11, while the Plantower normalized  
815 reported size distribution changed very little. Invariant Plantower size distributions were also  
816 observed during controlled laboratory studies (He et al., 2020; Kuula et al., 2020; Tryner et al.,  
817 2020). This suggests that the values in the channels above CH1 are software generated and  
818 indicates that the most relevant output from the PMS is from the CH1 channel. The bottom row

819 of Table S5 shows that the PMS bin fractions above 1  $\mu\text{m}$  increased by only a factor of 2–5 in a  
820 high- $\text{PM}_{2.5}$  windblown dust episode at Keeler, California. This is consistent with the PMS model  
821 prediction that PMS coarse aerosol response is small relative to a perfect nephelometer.

822 The results above indicate that CH1 is the primary source of aerosol information from the PMS  
823 sensor. Additionally, consistent with the sensor behaving like a cell-reciprocal nephelometer, it  
824 was found that CH1 was proportional to the aerosol scattering coefficient, not the number  
825 concentration of particles having diameters greater than 0.3  $\mu\text{m}$ . CH1 was approximately a  
826 factor of 10 lower than the DMPS number concentration for a similar size range.

### 827 **5.2.7 Relationship between CH1 and $\text{PM}_{2.5}$**

828 The  $\text{PM}_{2.5}$  mass concentration was not measured by Federal Reference Method (FRM) or Federal  
829 Equivalent Method (FEM) instruments at MLO and BOS during this study. Consequently, the  
830 PA-PMS  $\text{PM}_{2.5}$  or CH1 results cannot be compared with  $\text{PM}_{2.5}$  concentrations, but they can be  
831 compared with measured scattering coefficients and discussed in the context of mass scattering  
832 efficiency, which ties scattering coefficient to mass concentration.

833 Figure S19 shows that the PA-PMS  $\text{PM}_{2.5}$  channel is reasonably well correlated with  $b_{\text{sp}1}$  for  
834 values greater than about 10–20  $\mu\text{g m}^{-3}$ , typical of many moderately polluted locations, with a  
835 calculated mass scattering efficiency of approximately 2.5  $\text{m}^2 \text{g}^{-1}$ . This value of the mass  
836 scattering efficiency is at the low end of the range of values reported by Hand and Malm (2007),  
837 which could reflect the nature of the observed aerosols or an error of the PA-PMS  $\text{PM}_{2.5}$  mass  
838 concentration. This suggests that the effectiveness of the PA-PMS to serve as a  $\text{PM}_{2.5}$  mass  
839 concentration monitor is due both to the sensor behaving like an imperfect integrating  
840 nephelometer and to the mass scattering efficiency of ambient  $\text{PM}_{2.5}$  aerosols being roughly  
841 constant with values in the 2–4  $\text{m}^2 \text{g}^{-1}$  range. However, it is likely that the PA-PMS  
842 underestimates  $\text{PM}_{2.5}$  for very clean areas where  $b_{\text{sp}1}$  is often less than 10  $\text{Mm}^{-1}$ . For example, the  
843 PA-PMS  $\text{PM}_{2.5}$  was zero for 1099 of the hours in this study when  $b_{\text{sp}1}$  was greater than 1  $\text{Mm}^{-1}$ .

844 One may obtain a lower bound estimate of the PA-PMS RMSE 1 h average mass concentration  
845 from the study results. Figure 14 shows the PurpleAir scattering coefficient RMSE as a function  
846 of the measured scattering coefficient. For example, the PurpleAir NRMSE is 20% for a fine  
847 aerosol scattering coefficient of 25  $\text{Mm}^{-1}$ . For an aerosol having a mass scattering efficiency of  
848 2–3  $\text{m}^2 \text{g}^{-1}$ , this is approximately 10  $\mu\text{g m}^{-3}$ . Thus, the PurpleAir 1 h average RMSE is roughly 2  
849  $\mu\text{g m}^{-3}$ . This is somewhat lower than the reported mean absolute error of  $\sim 4 \mu\text{g m}^{-3}$  for hourly  
850 average  $\text{PM}_{2.5}$  in Pittsburgh (Malings et al., 2020). This error assumes that the mass scattering  
851 efficiency is fixed and known. This is generally not the case, and the actual error in the mass  
852 concentrations will be larger.

853 The mean 1 h average fine aerosol scattering coefficient  $b_{\text{sp}1}$  at MLO during our yearlong study  
854 was 1.50  $\text{Mm}^{-1}$ . From Fig. 14, the PurpleAir had a RMSE of 0.60  $\text{Mm}^{-1}$ . For an aerosol having a  
855 mass scattering efficiency of 2–3  $\text{m}^2 \text{g}^{-1}$ , this corresponds to a 1 h average RMSE of roughly 0.2–  
856 0.3  $\mu\text{g m}^{-3}$ . This is well below the advertised 1 h average MDL of commercial  $\text{PM}_{2.5}$  monitors.  
857 For example, the BAM 1020 specifies a typical hourly detection limit of 3.6  $\mu\text{g m}^{-3}$ .

## 858 **6. Summary, discussion, and future work**

859 We have demonstrated that the PMS sensor inside the PA monitor (PA-PMS) appears to behave  
860 as an imperfect reciprocal integrating nephelometer. As a scattering sensor, the PMS cannot  
861 directly count nor size particles in the air stream. The PMS uses an unknown algorithm to  
862 convert the scattering signal to a near-constant normalized number distribution from which PM  
863 concentrations are derived.

864 The scattering coefficient that is measured by an ideal integrating nephelometer does not need  
865 correction for any aerosol attributes such as shape, chemical composition, refractive index, or  
866 diameter. It is a valuable measure for visibility and global climate monitoring. Simple low-cost  
867 sensors such as the PA-PMS can play a role in estimating aerosol scattering coefficients and  
868 improving global coverage. Yearlong field data at NOAA's Mauna Loa Observatory and  
869 Boulder Table Mountain sites show that the 1 h average of the PA-PMS CH1 is highly correlated  
870 with a nephelometer-measured fine aerosol scattering coefficient at 550 nm,  $b_{sp1}$ , over a wide  
871 scattering coefficient range of  $0.4 \text{ Mm}^{-1}$  to  $500 \text{ Mm}^{-1}$ . The relationship between CH1 and  $b_{sp1}$  at  
872 550 nm is found to be  $b_{sp1} (\text{Mm}^{-1}) = 0.015 \times \text{CH1}$  when both quantities are adjusted to the same  
873 temperature and pressure.

874 The physical-optical model developed in this paper for the PMS and the general consistency with  
875 both published laboratory data for a variety of fine aerosols and ambient field data may motivate  
876 users of other low-cost sensors to develop similar models. It is possible that some of the other  
877 low-cost sensors also use polarized lasers in a cell-reciprocal configuration like the PMS. Such  
878 models would improve the understanding of sensor operation and help users better recognize the  
879 opportunities and limitations of other low-cost sensors in applications such as monitoring the  
880 scattering coefficient.

881 The strong relationship between  $b_{sp1}$  and CH1 and the general agreement between the model and  
882 published laboratory data support characterizing the PA-PMS as an imperfect truncated cell-  
883 reciprocal nephelometer. The results demonstrate that it is possible to use the PA-PMS to  
884 estimate the 1 h average fine aerosol scattering coefficient across a wide range of aerosol  
885 scattering concentrations, provided the aerosol median scattering diameter is between  $0.26 \mu\text{m}$   
886 and  $0.46 \mu\text{m}$ . The CH1 and  $b_{sp1}$  relationship is dependent on the size distribution, and it is  
887 expected to change for locations and times where the particle size shifts to larger or smaller sizes  
888 than those measured at BOS and MLO.

889 We found that the PA-PMS has important limitations compared to integrating nephelometers. It  
890 measures the light scattering over a smaller angular range, causing a significant truncation of the  
891 scattering signal in the forward and backward directions. Additionally, the PA-PMS uses a  
892 polarized light source; the sensor most likely does not have a cosine response; the laser beam  
893 profile is not a simple plane wave; and the inlet/geometry creates a broad uncertain particle size  
894 cut point. Nephelometers calibrate their scattering coefficient with  $\text{CO}_2$  or Suva, but the PMS is  
895 unresponsive to these gases. As a result, there is currently no convenient way to calibrate the  
896 PMS to ensure its accuracy. Neither PA nor Plantower provide technical support. Quality  
897 assurance and control are not as robust as one encounters for regulatory and scientific monitoring  
898 instruments. For this reason, it is useful to test the PMS sensors in filtered air before using them  
899 and to limit field use to those sensors that have 1 h average CH1 values less than 2. While

900 sampling, it is necessary to compare 1 h averages from the two PMS sensors in each PA monitor  
901 to become aware of any changes and, if needed, to replace them in a timely fashion.

902 This study limited its findings to low-RH air, because both the PA monitors and the  
903 nephelometers were heated to reduce RH. Since RH plays such an important role in water uptake  
904 by hygroscopic aerosols and the concomitant increase in the scattering coefficient, future work is  
905 planned to compare unheated PA monitors with an unheated nephelometer that does not reduce  
906 RH before sampling. Our model predicts that the PMS may not be as responsive to hygroscopic  
907 growth as an unheated nephelometer. This is a topic of current study.

908 The PA-PMS reports a mass concentration of PM<sub>2.5</sub> particles, and many papers have been written  
909 to compare the PA-PMS values with reference instruments and explain the observed differences.  
910 The modest agreement that has been reported is the direct result of two factors generally  
911 overlooked in those publications: the PA-PMS behaves like an imperfect integrating  
912 nephelometer that provides a representative value of the light scattering coefficient, and the mass  
913 scattering efficiency of PM<sub>2.5</sub> aerosols is roughly constant, with values in the 2–4 m<sup>2</sup> g<sup>-1</sup> range.

## 914 **Appendix**

915 The PMS physical-optical model makes some simplifying assumptions. The actual PMS laser  
916 beam profile is not a simple plane wave but complex in shape. The model assumes the laser is a  
917 plane wave with a constant laser beam irradiance profile. This allows the use of Mie theory to  
918 predict the light scattered by particles in the laser. Secondly, the model calculates the light  
919 scattered to a narrow strip across the middle instead of the entire photodiode. It assumes that the  
920 irradiance received by the narrow strip is representative of the entire photodiode.

921 The intensity of light scattered from a particle in the laser is

$$922 \quad I(\theta) = F_{dv} \beta(\theta) dv \quad (A1)$$

923 where  $I(\theta)$  is the intensity of light at angle  $\theta$  scattered from a particle in the volume element  $dv$   
924 (with units of Watt sr<sup>-1</sup>);  $\beta(\theta)$  is the volume scattering function (m<sup>-1</sup> sr<sup>-1</sup>);  $F_{dv}$  is the incident laser  
925 flux density (Watt m<sup>-2</sup>) impinging on the volume element  $dv$ ; and  $dv$  is the volume element  
926 within the laser.

927 The volume scattering function for a monodisperse aerosol having a diameter  $D_p$  and number  
928 concentration  $N(D_p)$  in the PMS laser is

$$929 \quad \beta(m, \lambda, \theta, D_p) = (\lambda/2\pi)^2 N(D_p) |S_1(m, \lambda, \theta, D_p)|^2 \quad (A2)$$

930 where  $|S_1(m, \lambda, \theta, D_p)|^2$  is the perpendicular scattering intensity function;  $\lambda$  is the laser  
931 wavelength;  $m$  is the particle complex refractive index;  $\theta$  is the scattering angle; and  $D_p$  is the  
932 aerosol diameter. Note that  $\theta = 0$  in the direction of the laser, and  $\theta = 90$  degrees perpendicular to  
933 the laser and photodiode.

934 For one particle of size  $D_p$  in the volume element  $dv$ ,  $N(D_p) dv = (1/dv) \times (dv) = 1$ .

935 The incremental power  $dP$  (Watt) scattered from a particle in the volume element  $dv$  across a  
 936 solid angle  $d\Omega$  subtended on the surface of a sphere at distance  $r$  from the particle, and normal to  
 937  $r$ , is

$$938 \quad dP = I(\theta) d\Omega. \quad (A3)$$

939  $d\Omega = dA_0 / r^2$ , where  $dA_0$  is the incremental area on the sphere at distance  $r$  from the particle and  
 940 normal to  $r$ .  $dP$  is then

$$941 \quad dP = I(\theta) dA_0 / r^2. \quad (A4)$$

942 For the PMS model,  $dA_0$  is a small rectangle with width  $w$  and height  $r d\theta$ , where  $w$  is the width  
 943 of the strip on the photodiode, and  $d\theta$  is the differential scattering angle.

944  $dA_0 = r d\theta \times w$ , where  $w$  is the width of the strip on the photodiode. From Fig. A1,  $r = b/\sin(\theta)$ ,  
 945 where  $b$  is the distance from the laser to the photodiode.

$$946 \quad d\Omega = dA_0 / r^2 = (r d\theta \times w) / r^2 = d\theta \times (w/r) = (w/b) \times \sin(\theta) d\theta. \quad (A5)$$

947 The incremental power across the solid angle  $d\Omega$  normal to  $r$  is then

$$948 \quad dP = I(\theta) \times dA_0 / r^2 = I(\theta) \times (w/b) \times \sin(\theta) d\theta. \quad (A6)$$

949 Substituting for  $I(\theta)$ ,

$$950 \quad dP(g,x,\theta) = [F_0 (\lambda/2\pi)^2 |S_1(\theta, D_p)|^2] \times (w/b) \times \sin(\theta) d\theta. \quad (A7)$$

951 Equation A7 can be further simplified by combining the constants into  $K = (\lambda/2\pi)^2 F_0 w/b$ , where  
 952  $K$  has units of watts:

$$953 \quad dP(g,x,\theta) = K |S_1(\theta, D_p)|^2 \sin(\theta) d\theta. \quad (A8)$$

954 The power received by the photodiode from a particle of diameter  $D_p$  in the volume element at  $x$   
 955 is obtained by numerically integrating across  $\theta$  on the photodiode:

$$956 \quad P(m, D_p) = K \int_{\theta_1(x)}^{\theta_2(x)} |S_1(m, \theta, D_p)|^2 \sin(\theta) d\theta. \quad (A9)$$

957 Due to the PMS geometry, the upper and lower angular scattering integration limits for  $\theta$  depend  
 958 on the location  $x$ . This can be seen in Fig. S4. For example, at  $x = 0$  mm, the upper and lower  
 959 integration limits for  $\theta$  are 18 to 38 degrees. At  $x = 4.0$  mm, over the center of the photodiode,  
 960 the angular integration limits are 50 to 130 degrees.

961 The total power  $P$  in Watts received by the photodiode from the light scattered by all the  
 962 particles of diameter  $D_p$  in the laser is obtained by carrying out the numerical integration in Eq.  
 963 A9 for all  $x$  from 0 to 10 mm:



964 
$$P(m, D_p) = K \int_{x=0}^{x=10mm} \int_{\theta_1(x)}^{\theta_2(x)} |S_1(m, \theta, D_p)|^2 \sin(\theta) d\theta dx. \quad (A10)$$

965 The result for carrying out this calculation for the power per particle of size  $D_p$  is in Table S6 for  
 966 wavelength 657 nm and particle refractive index 1.53+0.015i. The total power received at the  
 967 photodiode by a distribution of particles is obtained by summing up the power per particle of size  
 968  $D_p$  times the number of particles  $N(D_p, m)$  in the size interval  $D_p$  to  $D_p + dD_p$ .

969 
$$P = K \int_{D_p} \int_{x=0}^{x=10mm} \int_{\theta_1(x)}^{\theta_2(x)} |S_1(m, \theta, D_p)|^2 \sin(\theta) N(D_p, m) d\theta dx dD_p. \quad (A11)$$

970 Figure A1 shows the PMS geometry. The distance along the laser is the variable  $x$ , which ranges  
 971 from 0 to 10 mm. The distance along the photodiode is the variable  $g$ , which ranges from 0 to 3.0  
 972 mm. The distance between the photodiode and the laser is  $b$ , approximately 1.8 mm.

### 973 **Code and data availability**

974 Data sets are available on Zenodo.org. The dataset is available at  
 975 <https://doi.org/10.5281/zenodo.5764982>. The data were published on 15 December 2021.  
 976 Citation is: Ouimette, James; Malm, William; Schichtel, Bret; Sheridan Patrick; Andrews,  
 977 Elisabeth; Ogren, John A.; & Arnott, W. Patrick. (2021). Datasets for paper "Evaluating the  
 978 PurpleAir monitor as an aerosol light scattering instrument" (1.0\_20211215) [Data set]. Zenodo.  
 979 <https://doi.org/10.5281/zenodo.5764982>

### 980 **Supplement**

981 I think ACP fills out this - we have provided the supplement to them.

### 983 **Author contributions**

984 PJS and JRO designed the field study. PJS provided measurement data from the MLO and BOS  
 985 sites. BAS performed the uncertainty and precision analyses. WCM led the physical-optical  
 986 model development with BAS and JRO. JRO and WCM performed analysis of laboratory and  
 987 field data for model evaluation. WPA provided insight regarding the laser behavior and  
 988 instrument electronics. JAO and WCM independently performed the statistical analyses of the  
 989 TSI nephelometer and PA data. JAO and JRO performed measurements and tests to characterize  
 990 the PMS5003. EA led the manuscript submission and review process. All authors read and  
 991 commented on the article.

### 993 **Competing interests**

994 The authors declare that they have no conflict of interest.

### 996 **Acknowledgements**

997 The authors acknowledge the following for their contributions:  
 998 Jim Wendell, NOAA, for engineering support, Marty Martinsen, NOAA, for MLO field support,  
 999 Derek Hageman, CIRES, University of Colorado, for data acquisition and processing support,  
 1000 and Helene Bennett, CIRA, Colorado State University, for technical editing support. The

1001 National Park Service participation in this project was supported under the cooperative  
1002 agreement P17AC00971.

### 1003 **Disclaimer**

1004 The assumptions, findings, conclusions, judgments, and views presented herein are those of the  
1005 authors and should not be interpreted as necessarily representing NOAA or National Park  
1006 Service policies. Reference to any companies or specific commercial products does not  
1007 constitute endorsement by NOAA or the National Park Service.

### 1008 **References**

- 1009 Abu-Rahmah, A., Arnott, W. P., and Moosmuller, H.: Integrating nephelometer with a low  
1010 truncation angle and an extended calibration scheme, *Meas. Sci. Technol.* 17, 1723-1732, DOI  
1011 10.1088/0957-0233/17/7/010, 2006.
- 1012 Anderson, T. L. and Ogren, J. A.: Determining aerosol radiative properties using the TSI 3563  
1013 integrating nephelometer, *Aerosol Sci. Technol.*, 29, 57-69, DOI 10.1080/02786829808965551,  
1014 1998.
- 1015 Anderson, T. L., Covert, D. S., Marshall, S. F., Laucks, M. L., Charlson, R. J., Waggoner, A. P.,  
1016 Ogren, J. A., Caldow, R., Holm, R. L., Quant, F. R., Sem, G. J., Wiedensohler, A., Ahlquist, N.  
1017 A., and Bates, T. S.: Performance characteristics of a high-sensitivity, three-wavelength, total  
1018 scatter/backscatter nephelometer, *J. Atmos. Oceanic Technol.*, 13, 967-986, DOI 10.1175/1520-  
1019 0426(1996)013<0967:Pcoahs>2.0.Co;2, 1996.
- 1020 Andrews, E., Sheridan, P. J., Ogren, J. A., Hageman, D., Jefferson, A., Wendell, J., Alastuey, A.,  
1021 Alados-Arboledas, L., Bergin, M., Ealo, M., Hallar, A. G., Hoffer, A., Kalapov, I., Keywood,  
1022 M., Kim, J., Kim, S. W., Kolonjari, F., Labuschagne, C., Lin, N. H., Macdonald, A., Mayol-  
1023 Bracero, O. L., McCubbin, I. B., Pandolfi, M., Reisen, F., Sharma, S., Sherman, J. P., Sorribas,  
1024 M., and Sun, J. Y.: Overview of the NOAA/ESRL Federated Aerosol Network, *Bull. Am.*  
1025 *Meteorol. Soc.*, 100, 123-135, DOI 10.1175/bams-d-17-0175.1, 2019.
- 1026 Arnott, W. P., Walker, J. W., Moosmuller, H., Elleman, R. A., Jonsson, H. H., Buzorius, G.,  
1027 Conant, W. C., Flagan, R. C., and Seinfeld, J. H.: Photoacoustic insight for aerosol light  
1028 absorption aloft from meteorological aircraft and comparison with particle soot absorption  
1029 photometer measurements: DOE Southern Great Plains climate research facility and the coastal  
1030 stratocumulus imposed perturbation experiments, *J. Geophys. Res.-Atmospheres*, 111, DOI  
1031 10.1029/2005jd005964, 2006.
- 1032 Barkjohn, K. K., Gantt, B., and Clements, A. L.: Development and application of a United States  
1033 wide correction for PM<sub>2.5</sub> data collected with the PurpleAir Sensor, *Atmos. Meas. Tech.*  
1034 *Discuss.*, DOI <https://doi.org/10.5194/amt-2020-413>, 2020.
- 1035 Beuttell, R. G. and Brewer, A. W.: Instruments for the measurement of the visual range, *J. Sci.*  
1036 *Instr. Phys. Ind.*, 26, 357-359, DOI 10.1088/0950-7671/26/11/302, 1949.
- 1037 Bodhaine, B. A. and Mendonca, B. G.: Preliminary four wavelength nephelometer measurements  
1038 at Mauna Loa Observatory, *Geophys. Res. Lett.*, 1, 119-122, DOI 10.1029/GL001i003p00119,  
1039 1974.

- 1040 Bodhaine, B. A., Mendonca, B. G., Harris, J. M., and Miller, J. M.: Seasonal variations in  
1041 aerosols and atmospheric transmission at Mauna Loa Observatory, *J. Geophys. Res.-Oceans*, 86,  
1042 7395-7398, DOI 10.1029/JC086iC08p07395, 1981.
- 1043 Bohren, C. F. and Huffman, D. R.: *Absorption and Scattering of Light by Small Particles*, John  
1044 Wiley & Sons, Inc., New York, ISBN 0 471 057772 X, 1983.
- 1045 Brockman, J. E., Aerosol transport in lines and inlets - Sample extraction section 6.2 in *Aerosol*  
1046 *Measurement: Principles, Techniques and Applications, 3rd Edition*, Kulkarni, P., Baron, P., and  
1047 Willeke, K., eds., ISBN: 978-0-1033 470-38741-2, 2011.
- 1048 Butcher, S. S. and Charlson, R. J.: *An Introduction to Air Chemistry*, Academic Press,  
1049 <https://doi.org/10.1016/B978-0-12-148250-3.X5001-X>, ISBN 978-0-12-148250-3, 1972.
- 1050 Chambers, S. D., Zahorowski, W., Williams, A. G., Crawford, J., and Griffiths, A. D.:  
1051 Identifying tropospheric baseline air masses at Mauna Loa Observatory between 2004 and 2010  
1052 using Radon-222 and back trajectories, *J. Geophys. Res.-Atmospheres*, 118, 992-1004, DOI  
1053 10.1029/2012jd018212, 2013.
- 1054 Currie, L. A.: Limits for qualitative detection and quantitative determination - Application to  
1055 radiochemistry, *Anal. Chem.*, 40, 586-&, DOI 10.1021/ac60259a007, 1968.
- 1056 Friedlander, S. K.: *Smoke, Dust and Haze: Fundamentals of Aerosol Behavior*, Wiley, New  
1057 York, 333 pp., ISBN 10: 0471014680,13: 9780471014683, 1977.
- 1058 Gliss, J., Mortier, A., Schulz, M., Andrews, E., Balkanski, Y., Bauer, S. E., Benedictow, A. M.  
1059 K., Bian, H., Checa-Garcia, R., Chin, M., Ginoux, P., Griesfeller, J. J., Heckel, A., Kipling, Z.,  
1060 Kirkevåg, A., Kokkola, H., Laj, P., Le Sager, P., Lund, M. T., Myhre, C. L., Matsui, H., Myhre,  
1061 G., Neubauer, D., van Noije, T., North, P., Olivi, D. J. L., Remy, S., Sogacheva, L., Takemura,  
1062 T., Tsigaridis, K., and Tsyro, S. G.: AeroCom phase III multi-model evaluation of the aerosol  
1063 life cycle and optical properties using ground- and space-based remote sensing as well as surface  
1064 in situ observations, *Atmos. Chem. Phys.*, 21, 87-128, DOI 10.5194/acp-21-87-2021, 2021.
- 1065 Grinshpun, S., Willeke, K., and Kalatoor, S.: A general equation for aerosol aspiration by thin-  
1066 walled sampling probes in calm and moving air, *Atmos. Environ. Part a-General Topics*, 27,  
1067 1459-1470, DOI 10.1016/0960-1686(93)90132-i, 1993.
- 1068 Gupta, P., Doraiswamy, P., Levy, R., Pikelnaya, O., Maibach, J., Feenstra, B., Polidori, A.,  
1069 Kiros, F., and Mills, K. C.: Impact of California fires on local and regional air quality: The role  
1070 of a low-cost sensor network and satellite observations, *Geohealth*, 2, 172-181, DOI  
1071 10.1029/2018gh000136, 2018.
- 1072 Hagan, D. H. and Kroll, J. H.: Assessing the accuracy of low-cost optical particle sensors using a  
1073 physics-based approach, *Atmos. Meas. Tech.*, 13, 6343-6355, DOI 10.5194/amt-13-6343-2020,  
1074 2020.
- 1075 Hand, J. L., and Malm, W. C.: Review of aerosol mass scattering efficiencies from ground-based  
1076 measurements since 1990, *J. Geophys. Res.*, 112, D16203, doi:10.1029/2007JD008484, 2007.
- 1077 Hangal, S. and Willeke, K.: Aspiration efficiency - Unified model for all forward sampling  
1078 angles, *Environ. Sci. Technol.*, 24, 688-691, DOI 10.1021/es00075a012, 1990.

1079 Harris, J. M. and Kahl, J. D.: A descriptive atmospheric transport climatology for the Mauna Loa  
1080 Observatory, using clustered trajectories, *J. Geophys. Res.-Atmospheres*, 95, 13651-13667, DOI  
1081 10.1029/JD095iD09p13651, 1990.

1082 He, M. L., Kuerbanjiang, N., and Dhaniyala, S.: Performance characteristics of the low-cost  
1083 plantower PMS optical sensor, *Aerosol Sci. Technol.*, 54, 232-241, DOI  
1084 10.1080/02786826.2019.1696015, 2020.

1085 Heintzenberg, J. and Charlson, R. J.: Design and applications of the integrating nephelometer: A  
1086 review, *J. Atmos. Oceanic Technol.*, 13, 987-1000, DOI 10.1175/1520-  
1087 0426(1996)013<0987:Daaoiti>2.0.Co;2, 1996.

1088 Heintzenberg, J., Wiedensohler, A., Tuch, T. M., Covert, D. S., Sheridan, P., Ogren, J. A., Gras,  
1089 J., Nessler, R., Kleefeld, C., Kalivitis, N., Aaltonen, V., Wilhelm, R. T., and Havlicek, M.:  
1090 Intercomparisons and aerosol calibrations of 12 commercial integrating nephelometers of three  
1091 manufacturers, *J. Atmos. Oceanic Technol.*, 23, 902-914, DOI 10.1175/jtech1892.1, 2006.

1092 Hering, S. V.: Impactors, cyclones, and other inertial and gravitational collectors, in *Air*  
1093 *Sampling Instruments for Evaluation of Atmospheric Contaminants*, Cohen, B.S., Hering, S.V.  
1094 (eds.), proceedings of the American Conference of Governmental Industrial Hygienists,  
1095 Cincinnati, 279-289, ISBN 1882417089 9781882417087,  
1096 <http://calliope.dem.uniud.it/CLASS/DES-IND-PLA1/impactorscyclonesch14p1.pdf>, 1995.

1097 Holder, A. L., Mebust, A. K., Maghran, L. A., McGown, M. R., Stewart, K. E., Vallano, D. M.,  
1098 Elleman, R. A., and Baker, K. R.: Field evaluation of low-cost particulate matter sensors for  
1099 measuring wildfire smoke, *Sensors*, 20, 17, DOI 10.3390/s20174796, 2020.

1100 Hyslop, N. P. and White, W. H.: An empirical approach to estimating detection limits using  
1101 collocated data, *Environ. Sci. Technol.*, 42, 5235-5240, DOI 10.1021/es7025196, 2008.

1102 Hyslop, N. P. and White, W. H.: Estimating precision using duplicate measurements, *J. Air*  
1103 *Waste Manage. Assoc.*, 59, 1032-1039, DOI 10.3155/1047-3289.59.9.1032, 2009.

1104 Jayaratne, R., Liu, X. T., Ahn, K. H., Asumadu-Sakyi, A., Fisher, G., Gao, J., Mabon, A.,  
1105 Mazaheri, M., Mullins, B., Nyaku, M., Ristovski, Z., Scorgie, Y., Thai, P., Dunbabin, M., and  
1106 Morawska, L.: Low-cost PM<sub>2.5</sub> sensors: An assessment of their suitability for various  
1107 applications, *Aerosol Air Qual. Res.*, 20, 520-532, DOI 10.4209/aaqr.2018.10.0390, 2020.

1108 JCGM100:GUM: Evaluation of measurement data — Guide to the Expression of Uncertainty in  
1109 Measurement, International Standardization Organization, Geneva, accessed 22 March 2021,  
1110 <https://www.bipm.org/en/publications/guides/gum.html>, 2008.

1111 Kelly, K. E., Whitaker, J., Petty, A., Widmer, C., Dybwad, A., Sleeth, D., Martin, R., and  
1112 Butterfield, A.: Ambient and laboratory evaluation of a low-cost particulate matter sensor,  
1113 *Environ. Pollut.*, 221, 491-500, DOI 10.1016/j.envpol.2016.12.039, 2017.

1114 Kuula, J., Makela, T., Aurela, M., Teinila, K., Varjonen, S., Gonzalez, O., and Timonen, H.:  
1115 Laboratory evaluation of particle-size selectivity of optical low-cost particulate matter sensors,  
1116 *Atmos. Meas. Tech.*, 13, 2413-2423, DOI 10.5194/amt-13-2413-2020, 2020.

1117 Laj, P., Bigi, A., Rose, C., Andrews, E., Myhre, C. L., Collaud Coen, M., Lin, Y., Wiedensohler,  
1118 A., Schulz, M., Ogren, J. A., Fiebig, M., Gliss, J., Mortier, A., Pandolfi, M., Petaja, T., Kim, S.  
1119 W., Aas, W., Putaud, J. P., Mayol-Bracero, O., Keywood, M., Labrador, L., Aalto, P., Ahlberg,

1120 E., Arboledas, L. A., Alastuey, A., Andrade, M., Artinano, B., Ausmeel, S., Arsov, T., Asmi, E.,  
1121 Backman, J., Baltensperger, U., Bastian, S., Bath, O., Beukes, J. P., Brem, B. T., Bukowiecki,  
1122 N., Conil, S., Couret, C., Day, D., Dayantolis, W., Degorska, A., Eleftheriadis, K., Fetfatzis, P.,  
1123 Favez, O., Flentje, H., Gini, M. I., Gregoric, A., Gysel-Beer, M., Hallar, A. G., Hand, J., Hoffer,  
1124 A., Hueglin, C., Hooda, R. K., Hyvarinen, A., Kalapov, I., Kalivitis, N., Kasper-Giebl, A., Kim,  
1125 J. E., Kouvarakis, G., Kranjc, I., Krejci, R., Kulmala, M., Labuschagne, C., Lee, H. J.,  
1126 Lihavainen, H., Lin, N. H., Loschau, G., Luoma, K., Marinoni, A., Dos Santos, S. M.,  
1127 Meinhardt, F., Merkel, M., Metzger, J. M., Mihalopoulos, N., Nguyen, N. A., Ondracek, J.,  
1128 Perez, N., Perrone, M. R., Petit, J. E., Picard, D., Pichon, J. M., Pont, V., Prats, N., Prenni, A.,  
1129 Reisen, F., Romano, S., Sellegri, K., Sharma, S., Schauer, G., Sheridan, P., Sherman, J. P.,  
1130 Schutze, M., Schwerin, A., Sohmer, R., Sorribas, M., Steinbacher, M., Sun, J. Y., Titos, G.,  
1131 Toczko, B., Tuch, T., Tulet, P., Tunved, P., Vakkari, V., Velarde, F., Velasquez, P., Villani, P.,  
1132 Vratolis, S., Wang, S. H., Weinhold, K., Weller, R., Yela, M., Yus-Diez, J., Zdimal, V., Zieger,  
1133 P., and Zikova, N.: A global analysis of climate-relevant aerosol properties retrieved from the  
1134 network of Global Atmosphere Watch (GAW) Near-Surface Observatories, *Atmos. Meas. Tech.*,  
1135 13, 4353-4392, DOI 10.5194/amt-13-4353-2020, 2020.

1136 Malings, C., Tanzer, R., Hauryliuk, A., Saha, P. K., Robinson, A. L., Presto, A. A., and  
1137 Subramanian, R.: Fine particle mass monitoring with low-cost sensors: Corrections and long-  
1138 term performance evaluation, *Aerosol Sci. Technol.*, 54, 160-174, DOI  
1139 10.1080/02786826.2019.1623863, 2020.

1140 Malm, W. C., Sisler, J. F., Huffman, D., Eldred, R. A., and Cahill, T. A.: Spatial and seasonal  
1141 trends in particle concentration and optical extinction in the United States, *J. Geophys. Res.*, 99,  
1142 1347-1370, DOI 10.1029/93JD02916, 1994.

1143 Markowicz, K. M. and Chilinski, M. T.: Evaluation of two low-cost optical particle counters for  
1144 the measurement of ambient aerosol scattering coefficient and angstrom ngstrom exponent,  
1145 *Sensors*, 20, DOI 10.3390/s20092617, 2020.

1146 Mehadi, A., Moosmueller, H., Campbell, D. E., Ham, W., Schweizer, D., Tarnay, L., and Hunter,  
1147 J.: Laboratory and field evaluation of real-time and near real-time PM<sub>2.5</sub> smoke monitors, *J. Air  
1148 Waste Manage. Assoc.*, 70, 158-179, DOI 10.1080/10962247.2019.1654036, 2020.

1149 Middleton, W. E. K.: *Vision Through the Atmosphere*, University of Toronto Press, Toronto,  
1150 250 pp., ISBN 1487587104, 9781487587109, 1952.

1151 Miller, J. M.: A 5-year climatology of back trajectories from the Mauna Loa Observatory,  
1152 Hawaii, *Atmos. Environ.*, 15, 1553-1558, DOI 10.1016/0004-6981(81)90138-4, 1981.

1153 Molenaar, J. V.: Analysis of the real world performance of the Optec NGN-2 ambient  
1154 nephelometer, presented at the Air & Waste Management Association conference on Visual  
1155 Air Quality: Aerosols and Global Radiation Balance, Bartlett, New Hampshire, 9-12 September,  
1156 243-265, [https://www.optecinc.com/visibility/pdf/ngn\\_2\\_analysis\\_real\\_world.pdf](https://www.optecinc.com/visibility/pdf/ngn_2_analysis_real_world.pdf), 1997.

1157 Morawska, L., Thai, P. K., Liu, X. T., Asumadu-Sakyi, A., Ayoko, G., Bartonova, A., Bedini,  
1158 A., Chai, F. H., Christensen, B., Dunbabin, M., Gao, J., Hagler, G. S. W., Jayaratne, R., Kumar,  
1159 P., Lau, A. K. H., Louie, P. K. K., Mazaheri, M., Ning, Z., Motta, N., Mullins, B., Rahman, M.  
1160 M., Ristovski, Z., Shafiei, M., Tjondronegoro, D., Westerdahl, D., and Williams, R.:  
1161 Applications of low-cost sensing technologies for air quality monitoring and exposure

1162 assessment: How far have they gone?, *Environ. Int.*, 116, 286-299, DOI  
1163 10.1016/j.envint.2018.04.018, 2018.

1164 Mulholland, G. W. and Bryner, N. P.: Radiometric model of the transmission cell-reciprocal  
1165 nephelometer, *Atmos. Environ.*, 28, 873-887, DOI 10.1016/1352-2310(94)90246-1, 1994.

1166 Muller, T., Laborde, M., Kassell, G., and Wiedensohler, A.: Design and performance of a three-  
1167 wavelength LED-based total scatter and backscatter integrating nephelometer, *Atmos. Meas.*  
1168 *Tech.*, 4, 1291-1303, DOI 10.5194/amt-4-1291-2011, 2011.

1169 Nakayama, T., Suzuki, H., Kagamitani, S., Ikeda, Y., Uchiyama, A., and Matsumi, Y.:  
1170 Characterization of a three wavelength Photoacoustic Soot Spectrometer (PASS-3) and a  
1171 Photoacoustic Extinctionmeter (PAX), *J. Meteorol. Soc. Jpn.*, 93, 285-308, DOI  
1172 10.2151/jmsj.2015-016, 2015.

1173 Naqwi, A. and Durst, F.: Focusing of diode laser beams - A simple mathematical model, *Appl.*  
1174 *Optics*, 29, 1780-1785, DOI 10.1364/ao.29.001780, 1990.

1175 Pandolfi, M., Alados-Arboledas, L., Alastuey, A., Andrade, M., Angelov, C., Artinano, B.,  
1176 Backman, J., Baltensperger, U., Bonasoni, P., Bukowiecki, N., Coen, M. C., Conil, S., Coz, E.,  
1177 Crenn, V., Dudoitis, V., Ealo, M., Eleftheriadis, K., Favez, O., Fetfatzis, P., Fiebig, M., Flentje,  
1178 H., Ginot, P., Gysel, M., Henzing, B., Hoffer, A., Smejkalova, A. H., Kalapov, I., Kalivitis, N.,  
1179 Kouvarakis, G., Kristensson, A., Kulmala, M., Lihavainen, H., Lunder, C., Luoma, K., Lyamani,  
1180 H., Marinoni, A., Mihalopoulos, N., Moerman, M., Nicolas, J., O'Dowd, C., Petaja, T., Petit, J.  
1181 E., Pichon, J. M., Prokopiuk, N., Putaud, J. P., Rodriguez, S., Sciare, J., Sellegri, K., Swietlicki,  
1182 E., Titos, G., Tuch, T., Tunved, P., Ulevicius, V., Vaishya, A., Vana, M., Virkkula, A., Vratolis,  
1183 S., Weingartner, E., Wiedensohler, A., and Laj, P.: A European aerosol phenomenology-6:  
1184 Scattering properties of atmospheric aerosol particles from 28 ACTRIS sites, *Atmos. Chem.*  
1185 *Phys.*, 18, 7877-7911, DOI 10.5194/acp-18-7877-2018, 2018.

1186 Papapostolou, V., Zhang, H., Feenstra, B. J., and Polidori, A.: Development of an environmental  
1187 chamber for evaluating the performance of low-cost air quality sensors under controlled  
1188 conditions, *Atmos. Environ.*, 171, 82-90, DOI 10.1016/j.atmosenv.2017.10.003, 2017.

1189 Pawar, H. and Sinha, B.: Humidity, density, and inlet aspiration efficiency correction improve  
1190 accuracy of a low-cost sensor during field calibration at a suburban site in the North-Western  
1191 Indo-Gangetic plain (NW-IGP), *Aerosol Sci. Technol.*, 54, 685-703, DOI  
1192 10.1080/02786826.2020.1719971, 2020.

1193 Ryan, S.: The wind field around Mauna Loa derived from surface and balloon observations, *J.*  
1194 *Geophys. Res.-Atmospheres*, 102, 10711-10725, DOI 10.1029/97jd00646, 1997.

1195 Sayahi, T., Butterfield, A., and Kelly, K. E.: Long-term field evaluation of the Plantower PMS  
1196 low-cost particulate matter sensors, *Environ. Pollut.*, 245, 932-940, DOI  
1197 10.1016/j.envpol.2018.11.065, 2019.

1198 Shaw, G. E.: Transport of Asian desert aerosol to the Hawaiian Islands, *J. Appl. Meteorol.*, 19,  
1199 1254-1259, DOI 10.1175/1520-0450(1980)019<1254:Toadat>2.0.Co;2, 1980.

1200 Sherman, J. P., Sheridan, P. J., Ogren, J. A., Andrews, E., Hageman, D., Schmeisser, L.,  
1201 Jefferson, A., and Sharma, S.: A multi-year study of lower tropospheric aerosol variability and  
1202 systematic relationships from four North American regions, *Atmos. Chem. Phys.*, 15, 12487-  
1203 12517, DOI 10.5194/acp-15-12487-2015, 2015.

1204 Snider, G., Weagle, C. L., Martin, R. V., van Donkelaar, A., Conrad, K., Cunningham, D.,  
1205 Gordon, C., Zwicker, M., Akoshile, C., Artaxo, P., Anh, N. X., Brook, J., Dong, J., Garland, R.  
1206 M., Greenwald, R., Griffith, D., He, K., Holben, B. N., Kahn, R., Koren, I., Lagrosas, N., Lestari,  
1207 P., Ma, Z., Martins, J. V., Quel, E. J., Rudich, Y., Salam, A., Tripathi, S. N., Yu, C., Zhang, Q.,  
1208 Zhang, Y., Brauer, M., Cohen, A., Gibson, M. D., and Liu, Y.: SPARTAN: a global network to  
1209 evaluate and enhance satellite-based estimates of ground-level particulate matter for global  
1210 health applications, *Atmos. Meas. Tech.*, 8, 505-521, DOI 10.5194/amt-8-505-2015, 2015.

1211 Tryner, J., L'Orange, C., Mehaffy, J., Miller-Lionberg, D., Hofstetter, J. C., Wilson, A., and  
1212 Volckens, J.: Laboratory evaluation of low-cost PurpleAir PM monitors and in-field correction  
1213 using co-located portable filter samplers, *Atmos. Environ.*, 220, DOI  
1214 10.1016/j.atmosenv.2019.117067, 2020.

1215 Zheng, T. S., Bergin, M. H., Johnson, K. K., Tripathi, S. N., Shirodkar, S., Landis, M. S.,  
1216 Sutaria, R., and Carlson, D. E.: Field evaluation of low-cost particulate matter sensors in high-  
1217 and low-concentration environments, *Atmos. Meas. Tech.*, 11, 4823-4846, DOI 10.5194/amt-11-  
1218 4823-2018, 2018.

1219 Zhou, Y.: Product data manual of PLANTOWER - PMS5003 series,  
1220 [https://www.aqmd.gov/docs/default-source/aq-spec/resources-page/plantower-pms5003-](https://www.aqmd.gov/docs/default-source/aq-spec/resources-page/plantower-pms5003-manual_v2-3.pdf)  
1221 [manual\\_v2-3.pdf](https://www.aqmd.gov/docs/default-source/aq-spec/resources-page/plantower-pms5003-manual_v2-3.pdf), accessed 15 March 2021, 2016.

1222

1223 **Tables**

1224 **Table 1.** Summary of PA, TSI nephelometer, and DMPS data coverage.

site	number of hours				percent coverage			Time period
	PA-PMS	TSI neph	DMPS	overlap	PA-PMS	TSI neph	DMPS	
<b>MLO</b>	9371	9204	na	9204	97.6	95.9	na	2019-05-06 to 2020-06-05
<b>BOS</b>	7716	7479	7045	6901	97.7	94.7	89.2	2020-02-13 to 2021-01-06

1225

1226

1227 **Table 2.** Summary of PA-PMS and nephelometer hourly observations at MLO and BOS.

Site	1 h median (average)				1 h range min-max			
	PA-PMS		TSI nephelometer		PA-PMS		TSI nephelometer	
	PM <sub>2.5</sub> μg m <sup>-3</sup>	CH1	b <sub>sp10</sub> Mm <sup>-1</sup>	b <sub>sp1</sub> Mm <sup>-1</sup>	PM <sub>2.5</sub> μg m <sup>-3</sup>	CH1	b <sub>sp10</sub> Mm <sup>-1</sup>	b <sub>sp1</sub> Mm <sup>-1</sup>
<b>MLO</b>	0.000 (0.12)	26.7 (75.2)	1.19 (2.82)	0.76 (1.50)	0.0 - 21.6	0.26 - 1649	-0.35 - 35.2	-0.29 - 34.2
<b>BOS</b>	3.37 (8.42)	720 (1422)	14.6 (32.4)	9.9 (20.9)	0.0 - 571	7.38 - 63340	-0.11 - 4097	-0.44 - 2596

1228

1229

1230 **Table 3.** Ordinary least square regression coefficients with a zero intercept and standard error for  
 1231 b<sub>sp1</sub> and CH1 as the dependent and independent variables, respectively, for the BOS, MLO, and  
 1232 combined datasets. CH1 and b<sub>sp1</sub> reported at STP. Also shown are the respective coefficients of  
 1233 determination, R<sup>2</sup>.

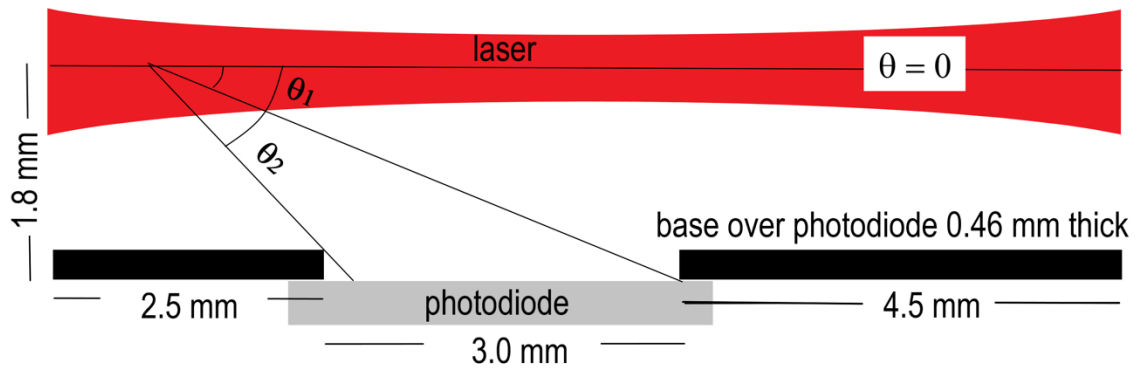
Site	slope (Mm <sup>-1</sup> )	standard error (Mm <sup>-1</sup> )	1/slope (Mm)	R <sup>2</sup>
<b>BOS</b>	0.015	2.68×10 <sup>-5</sup>	67.0	0.97
<b>MLO</b>	0.017	5.72×10 <sup>-5</sup>	59.0	0.85
<b>Both BOS&amp;MLO</b>	0.015	2.07×10 <sup>-5</sup>	67.0	0.97

1234

1235



1236 **Figures**

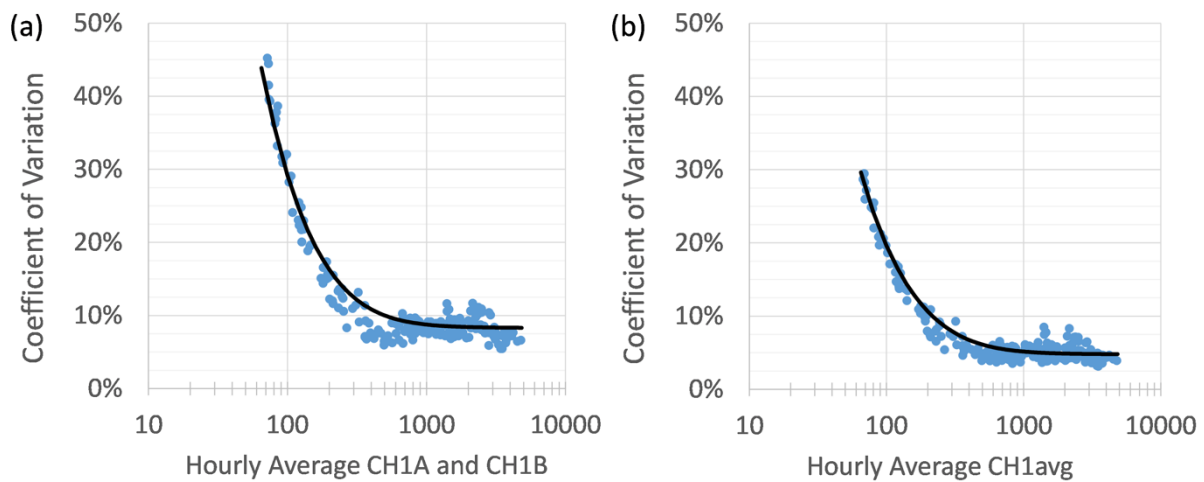


1237

1238 **Figure 1.** PMS sensor geometry highlighting the dimensions of laser beam (red) and photodiode  
1239 (gray) and the various relevant distances between the two.

1240

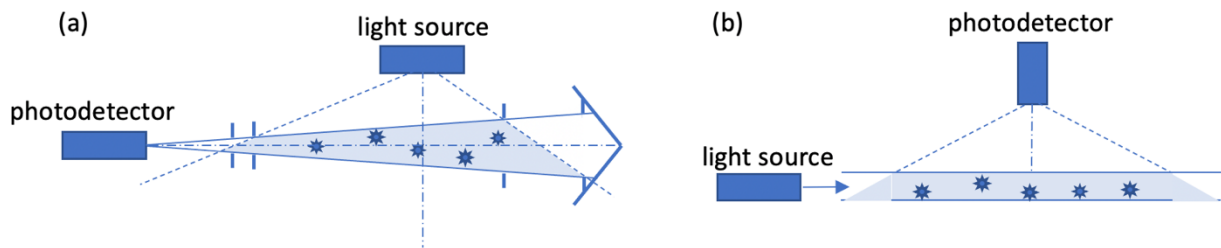
1241



1242

1243 **Figure 2.** Precision estimated as the coefficient of variation of the hourly CH1A and CH1B (a)  
1244 and CH1avg values (b) for the 19 collocated sensors and 9 PAs.

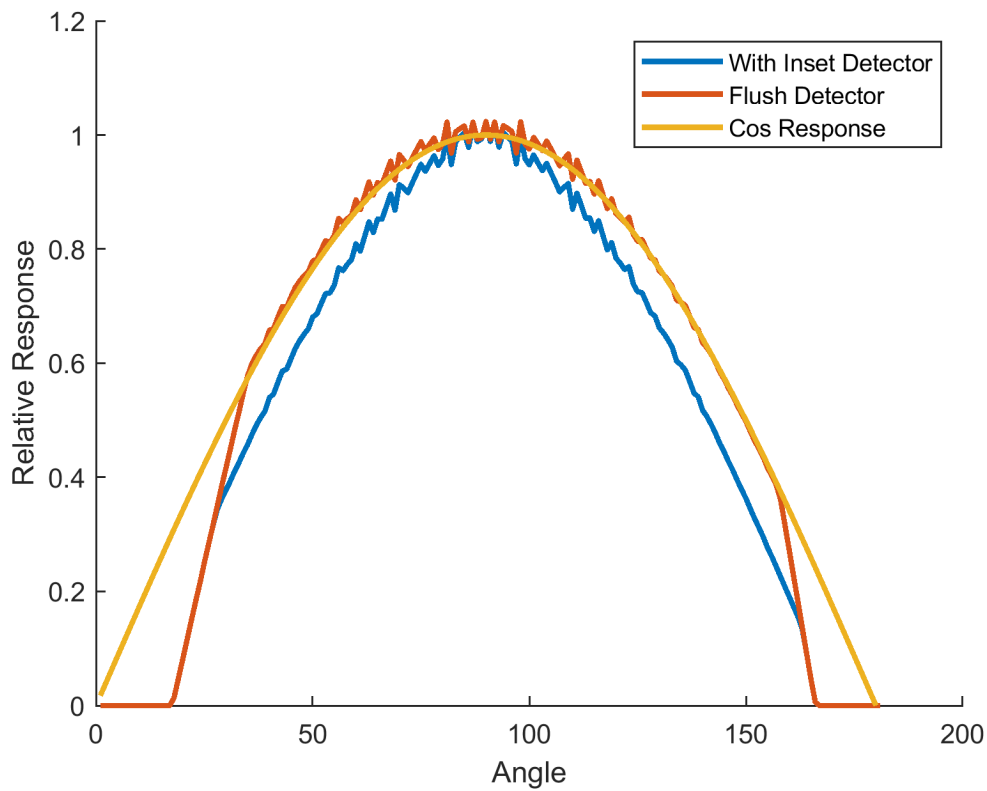
1245



1246

1247 **Figure 3.** Diagrams of the (a) cell-direct nephelometer and (b) cell-reciprocal nephelometer.

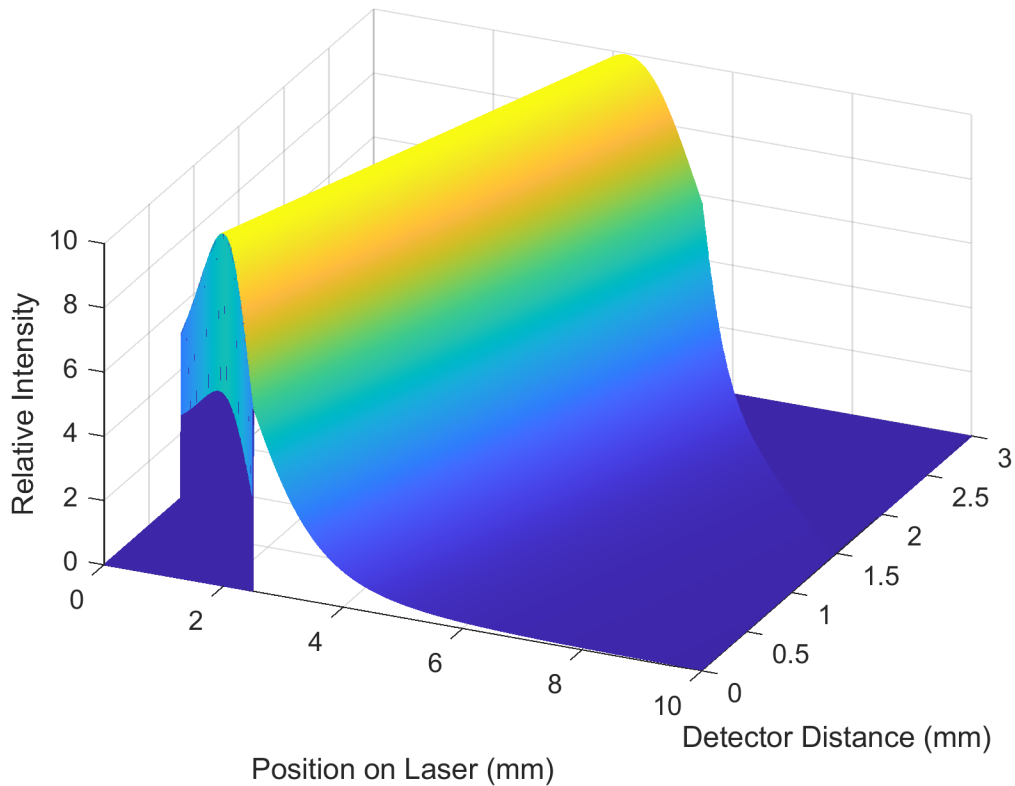
1248



1249

1250 **Figure 4.** Relative response of the photodetector resulting from truncated scattering angles and a  
 1251 recessed photodetector. See explanation of the different curves in text.

1252

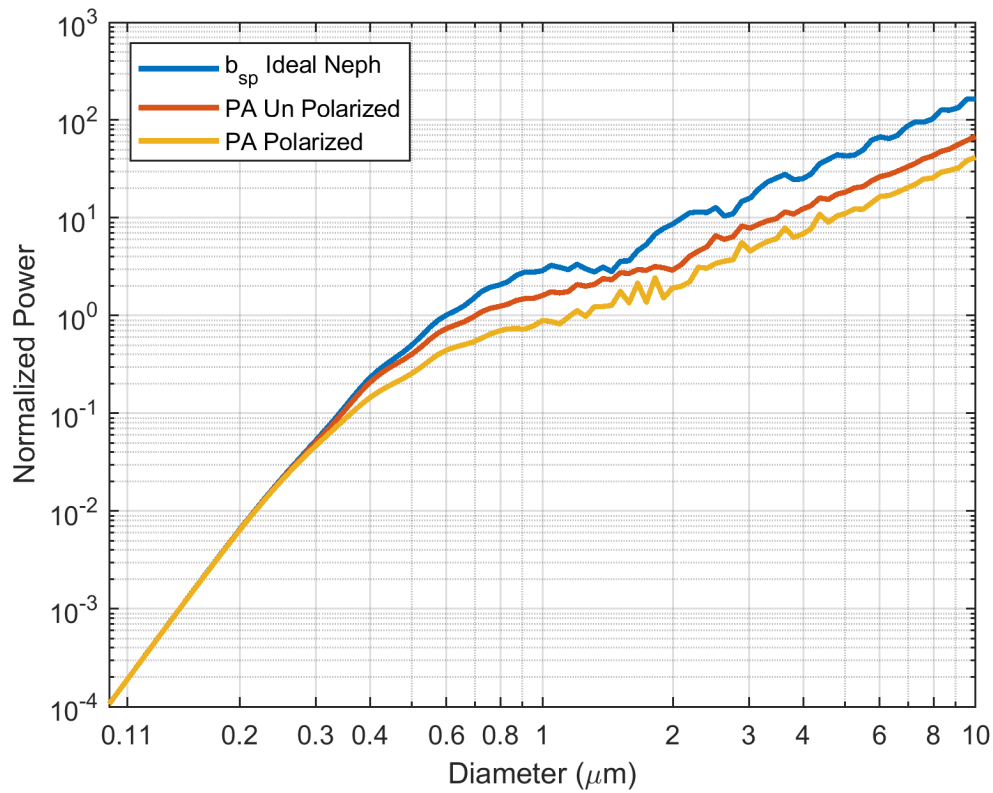


1253

Position on Laser (mm)

1254 **Figure 5.** Relative intensity of radiant energy scattered by a lognormally distributed aerosol  
 1255 volume size distribution with a volume mean diameter of  $0.33 \mu\text{m}$  and geometric standard  
 1256 deviation of 1.7 as a function of location of scattering event in the laser and as a function of  
 1257 position on the photodiode. Assumed laser wavelength was 650 nm, and the particle index of  
 1258 refraction was assumed to be 1.53. Positions in the laser and detector are from left to right as in  
 1259 Fig. 1 and are in units of mm.

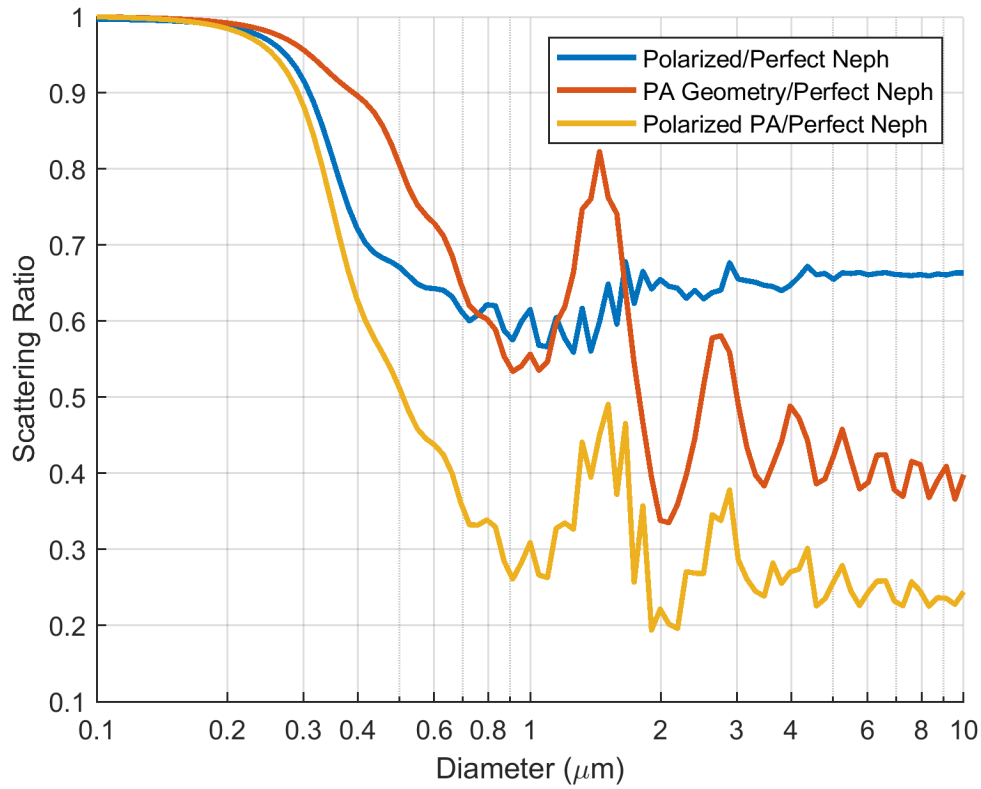
1260



1261

1262 **Figure 6.** Normalized power detected by an ideal integrating nephelometer, a PMS with an  
 1263 unpolarized light source, and a PMS with a perpendicularly polarized light source plotted as a  
 1264 function of particle diameter. Modeled light source wavelength is 657 nm, and the particle index  
 1265 of refraction is 1.53. See explanation of the different curves in text.

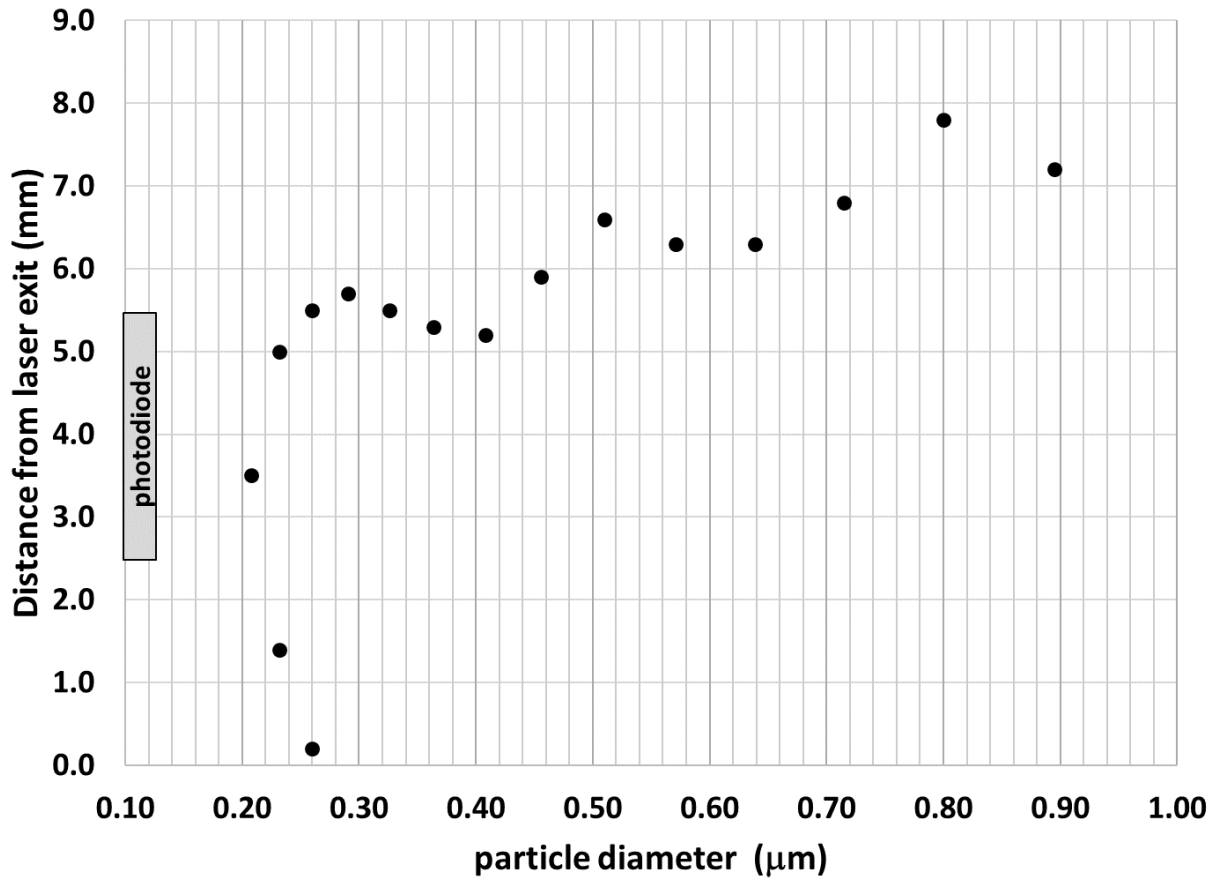
1266



1267

1268 **Figure 7.** Ratio of scattering of a “perfect” nephelometer to a nephelometer with a light source  
 1269 that is perpendicularly polarized (blue) and to a PMS with an unpolarized light source (red).  
 1270 Yellow line shows the effect of a perpendicularly polarized light source and PMS geometry. All  
 1271 three curves are plotted as a function of particle diameter.

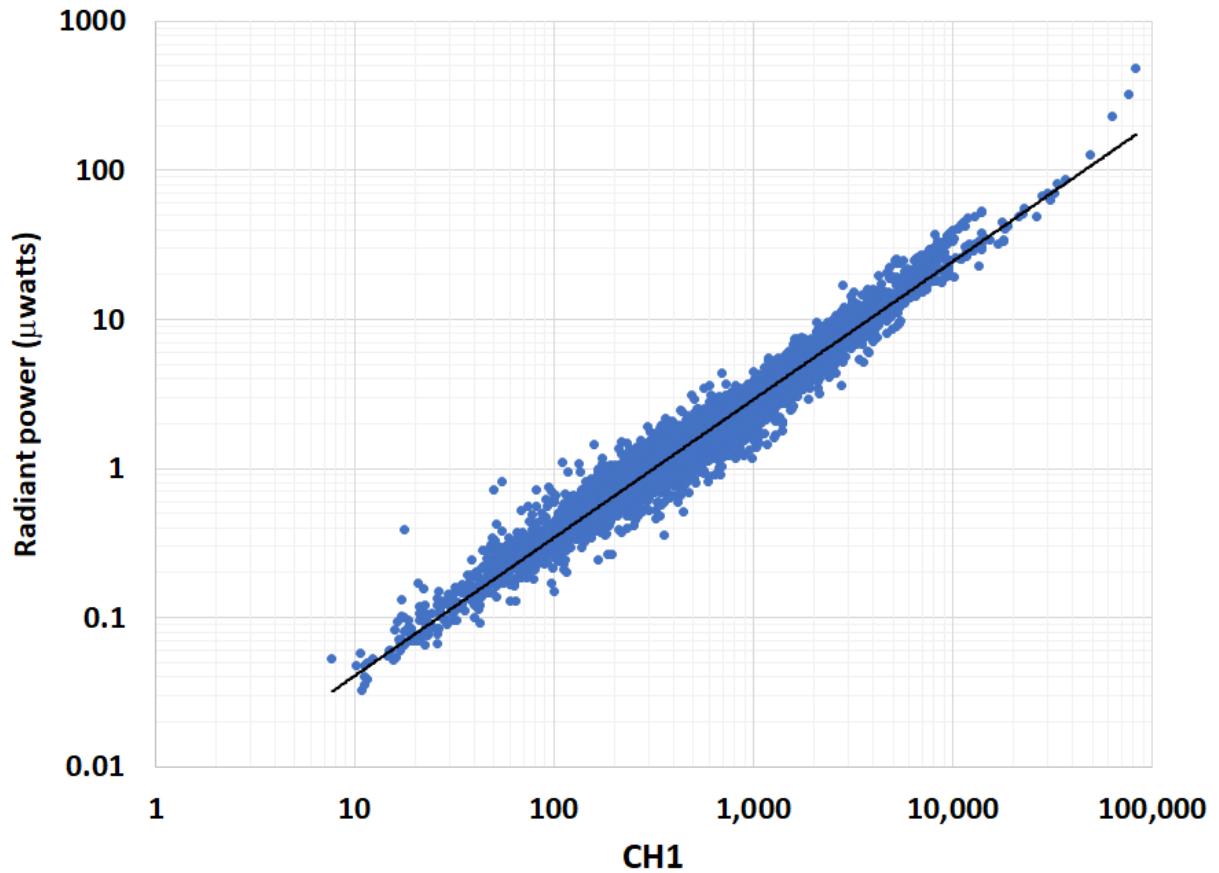
1272



1273

1274 **Figure 8.** The model predicts that different size particles can generate the same irradiance on the  
 1275 photodiode, depending on their location in the laser beam. In this example, each of the particles  
 1276 would create  $1.7 \times 10^{-2}$  picowatts of scattered irradiance on the photodiode.

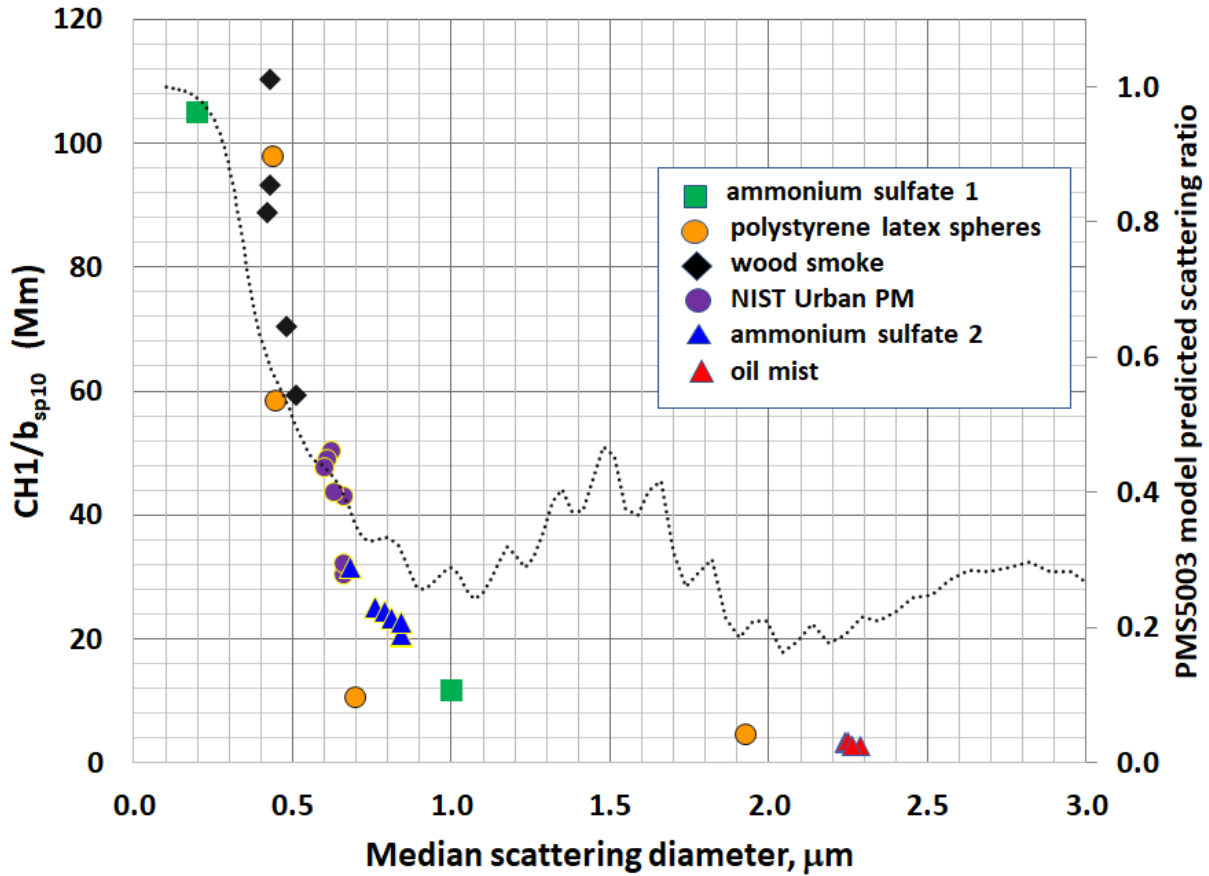
1277



1278

1279 **Figure 9.** One hour average CH1 reported values plotted against model-predicted radiant power  
1280 (or energy) in  $\mu\text{watts}$  on the photodiode. Both the CH1 and DMPS data were adjusted to STP  
1281 conditions. Ordinary least squares regression line is also shown. Plot is based on 6839 1 h  
1282 averages at BOS.

1283

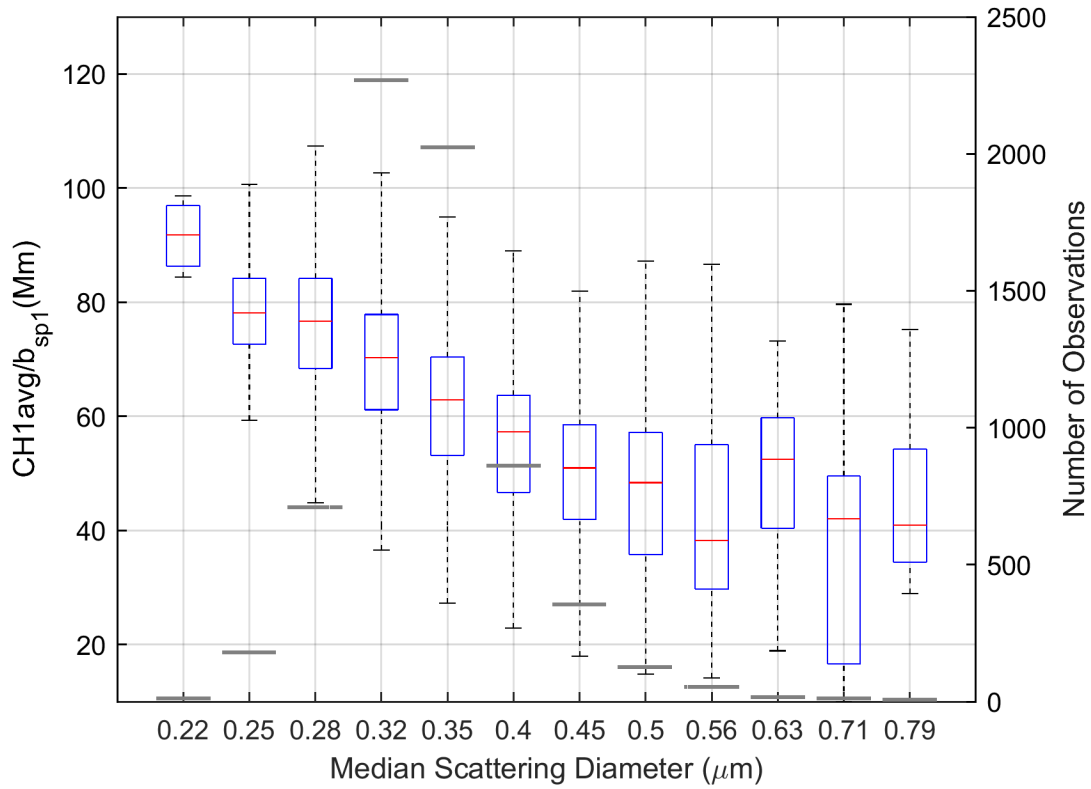


1284

1285 **Figure 10.** Laboratory measurements of  $CH1/b_{sp10}$  versus median scattering diameter from  
 1286 Tryner et al. (2020) and He et al. (2020). Results are compared with PMS physical-optical  
 1287 model prediction of the scattering ratio (yellow line in Fig. 7). Maximum value of 1.0 of the  
 1288 model-predicted scattering ratio is arbitrarily set at a  $CH1/b_{sp10}$  value of 110 Mm. Ammonium  
 1289 sulfate 1 data are from He et al. (2020); all other data are from Tryner et al. (2020).

1290

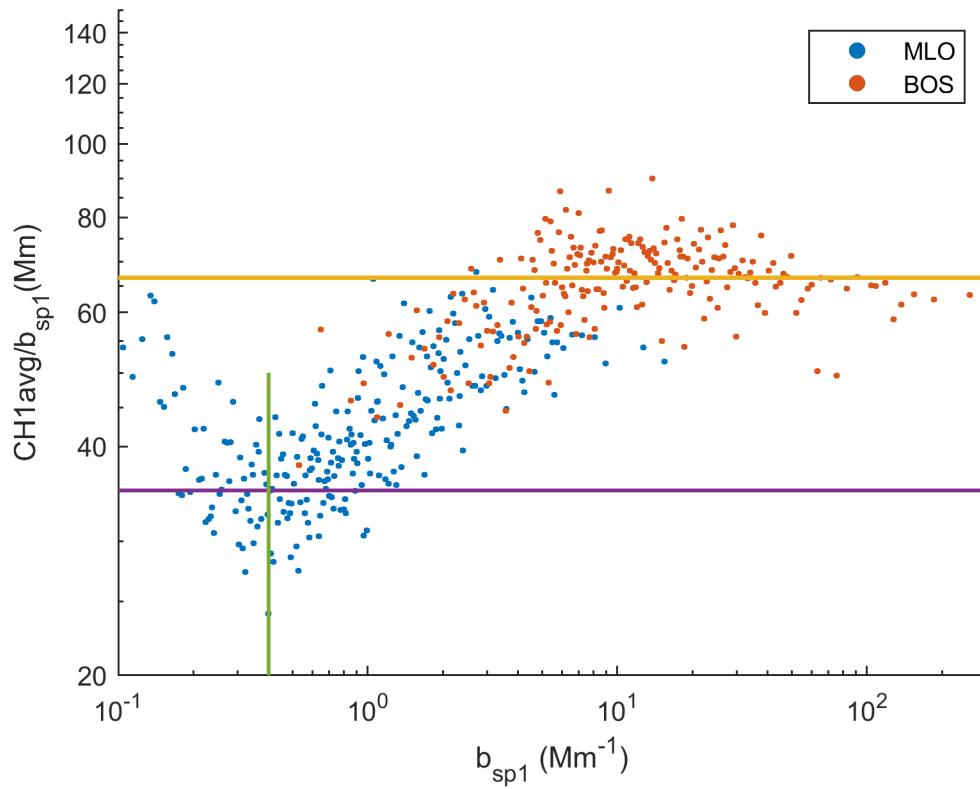




1291

1292 **Figure 11.** Observed decrease in  $\text{CH1avg}/b_{\text{sp1}}$  ratio as a function of MSD values. MSD values  
 1293 were selected based on a log scale but plotted equally spaced from each other to maintain  
 1294 uniformity in the dimensions of the box and whisker symbol. Red line represents the median  
 1295 value, and the bottom and top of each box are the first and third quartile values. Extremes shown  
 1296 on each box are the 2 and 98 percentiles. Black horizontal lines for each MSD value are the  
 1297 number of observations in the respective MSD bins.

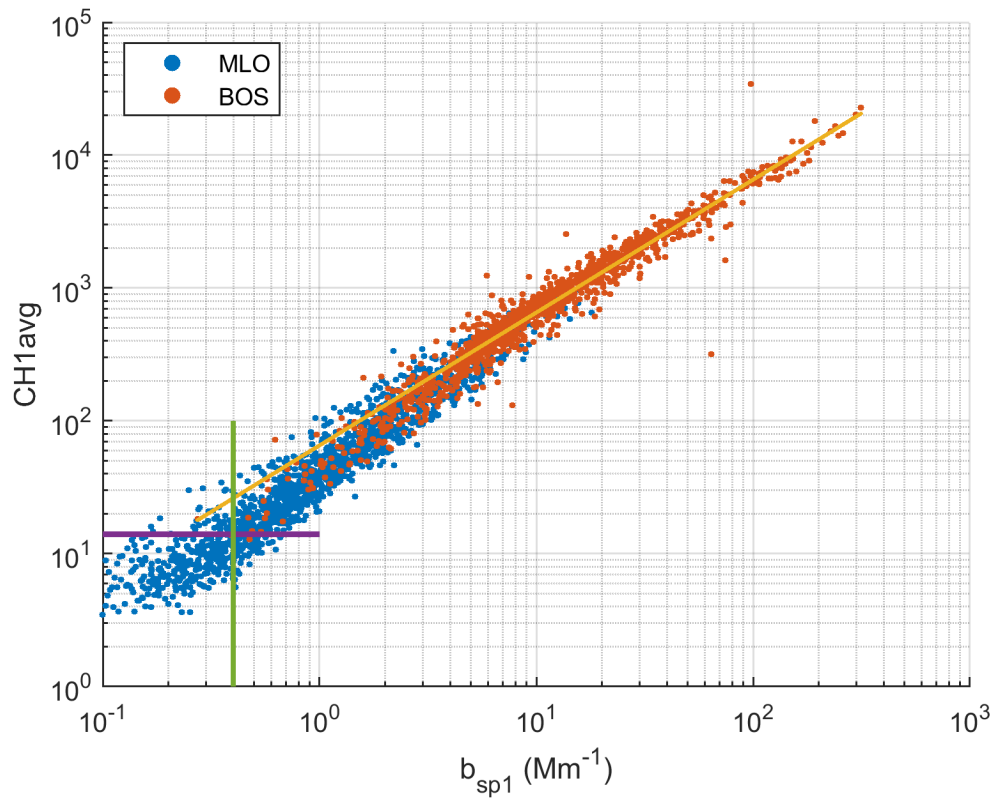
1298



1299

1300 **Figure 12.** Ratios of CH1avg and measured scattering,  $b_{sp1}$ , as a function of measured  $b_{sp1}$  for  
 1301 MLO and BOS. Green line corresponds to  $0.4 Mm^{-1}$  while the purple line, a ratio of 35 Mm,  
 1302 corresponds to the additive uncertainty of 14. Yellow line corresponds to a CH1avg/ $b_{sp1}$  ratio of  
 1303 approximately 67 Mm, the slope of CH1avg vs.  $b_{sp1}$  above about  $5 Mm^{-1}$ .

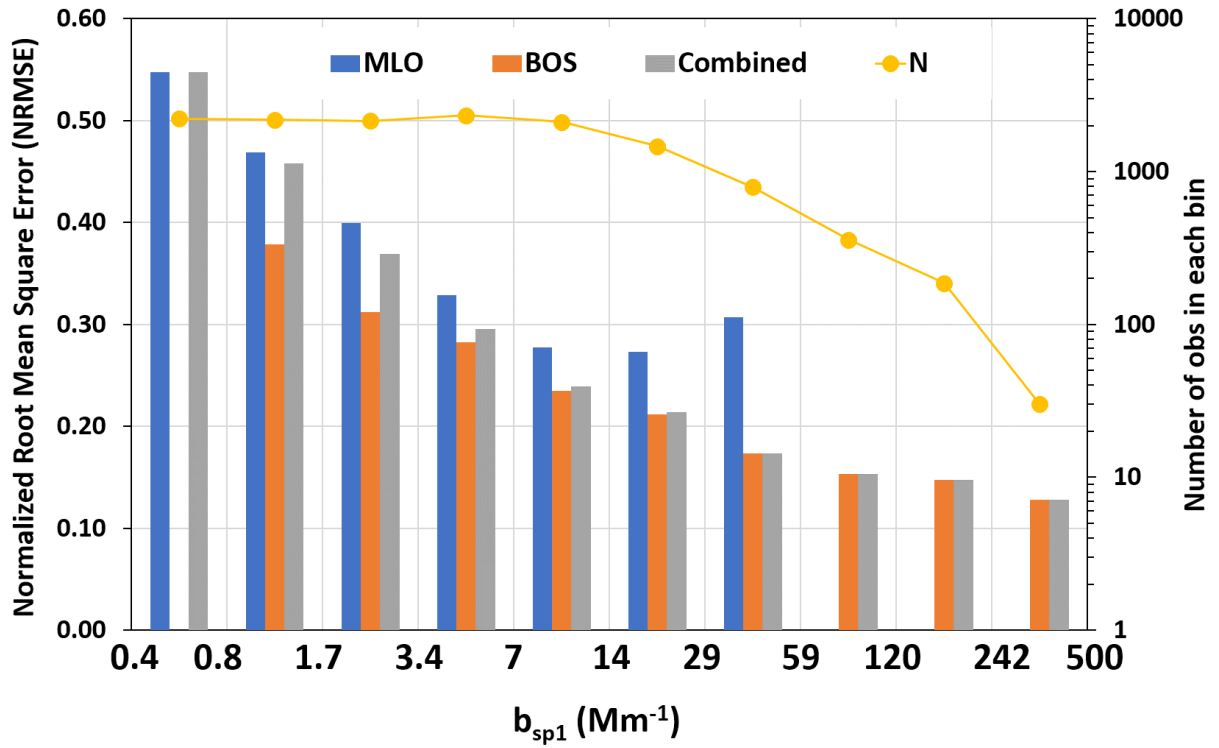
1304



1305

1306 **Figure 13.** Fine aerosol scattering coefficient from TSI nephelometer vs. CH1avg value from  
 1307 PA. Yellow line represents the fit to all data. Purple line shows the additive uncertainty of 14  
 1308 while b<sub>sp1</sub> values less than the green line were removed for the regression analysis.

1309



1310

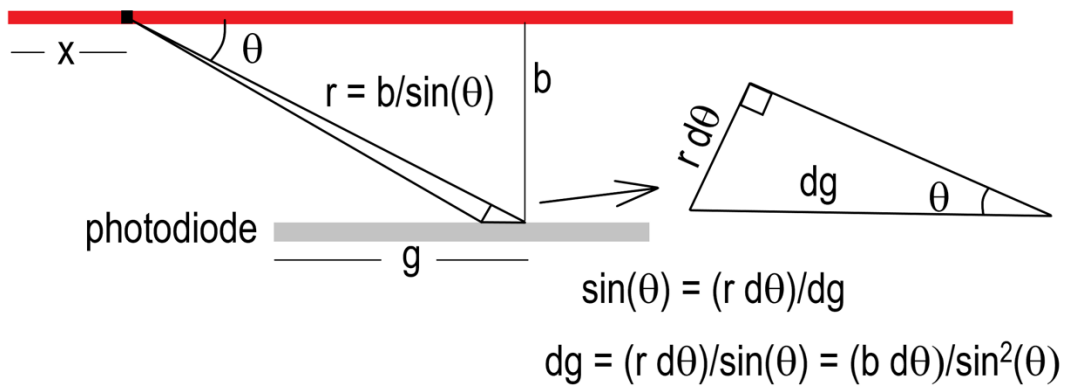
1311 **Figure 14.** Normalized root mean square error between measured and estimated scattering from  
 1312 CH1 values plotted as a function of binned  $b_{sp1}$  for the BOS, MLO, and combined datasets.

1313 Yellow line is referenced to the right axis to provide the number of observations in each bin.

1314 Numbers on the x-axis represent the lower and upper levels of each scattering bin.

1315

differential volume element at distance  $x$  along the laser,  
 scattering light at angle  $\theta$  to the photodiode



1316

1317 **Figure A1.** Sketch of PMS5003 geometry.

1318